

The Intergalactic Medium

Nicolas Tejos^a

^aInstituto de Física, Pontificia Universidad Católica de Valparaíso, Casilla 4059, Valparaíso, Chile

© 20xx Elsevier Ltd. All rights reserved.

This is a pre-print of a chapter for the Encyclopedia of Astrophysics (edited by I. Mandel, section editor S. McGee) to be published by Elsevier as a Reference Module.

Date: April 18, 2025

Nomenclature

AGN	Active galactic nuclei
BLA	Broad Lyman- α absorber
CGM	Circumgalactic medium
CIE	Collisional ionization equilibrium
CMB	Cosmic microwave background
COG	Curve of growth
DLA	Damped Lyman- α system
EoR	Epoch of Reionization
FRB	Fast radio burst
FWHM	Full width at half maximum
GRB	Gamma-ray burst
ICM	Intracluster medium
IGM	Intergalactic medium
IR	Infrared
ISM	Interstellar medium
Λ CDM	Λ cold dark matter
LLS	Lyman limit system
PIE	Photoionization equilibrium
SZ	Sunyaev-Zeldovich [effect]
UV	Ultraviolet
UVB	Ultraviolet background
WCGM	Warm circumgalactic medium
WHIM	Warm-hot intergalactic medium

Abstract

The intergalactic medium (IGM) comprises all the matter that lies between galaxies. Hosting the vast majority ($\gtrsim 90\%$) of the baryons in the Universe, the IGM is a critical reservoir and probe for cosmology and astrophysics, providing insights into large-scale structure formation and galaxy evolution. In this Chapter, we present an overview of the general properties of the IGM, focusing on their dependence on cosmic environment and cosmic time. Emphasis is given to the basic physical principles that allow us to model the density, temperature, and ionization state of the IGM, supported by results from cosmological hydrodynamical simulations. We also cover the foundational principles of quasar spectroscopy used to probe the IGM in absorption, with a particular focus on H I absorption lines. Finally, we briefly discuss future prospects and complementary observational techniques to enhance our understanding of the IGM.

Keywords: Intergalactic medium, galaxy evolution, large-scale structure of the Universe, quasar absorption line spectroscopy, Ly α forest

Learning objectives

This Chapter will help the readers to answer the following questions:

- What is the intergalactic medium (IGM) and what is its importance in astrophysics and cosmology?
- What is the composition and ionization state of the IGM?
- What are the different gas phases of the IGM?
- How do we model the ionization and thermal state of the IGM?
- How do the properties of the IGM change with cosmic environment and cosmic time?
- How do we observe the IGM using quasar spectroscopy?
- How do we model absorption lines in order to infer physical properties of the IGM?
- What are the different types of H I absorption line systems depending on their column density?
- How can we use these observational results to constrain physical parameters of the IGM?
- Are there other observational probes of the IGM besides quasar spectroscopy?

1 Introduction

1.1 Definition and general properties

The intergalactic medium (IGM) is defined as the baryonic matter and space that exists *between* galaxies; in this manner, the IGM definition is linked to that of galaxies. More fundamentally, the IGM and galaxies are indeed physically interlinked, such that they are affected by each other in their co-evolution across cosmic time and cosmic environments. Although the properties and nature of galaxies have been addressed extensively in the rest of this Encyclopedia, here we must emphasize that a well defined boundary between galaxy halos and the IGM does not exist. Therefore, we should be always cautious in how we establish the distinction between galaxies and the IGM, keeping in mind that this distinction may well depend on the particular study at hand.

Here we will adopt the terminology that the IGM corresponds to the diffuse medium outside dark matter halos of galaxies, as informed by current cosmological hydrodynamical simulations (see Section 2.4). In this manner, the interface between the IGM and galaxies is considered a different medium: the so-called circumgalactic medium (CGM). The CGM is sufficiently different and complex that has gained renewed attention, specially in the context of galaxy evolution (Tumlinson et al. 2017; Faucher-Giguère and Oh 2023; see also Chapter “Circumgalactic medium”).

Far away from galaxy halos, the typical densities of the IGM are comparable to the mean density of the Universe. On average, the IGM has a density of just one-fourth of an hydrogen atom per cubic meter (Section 2.3), far lower than the densities typically found within galaxies—for comparison, the typical density of the interstellar medium (ISM) is a few hydrogen atoms per cubic centimeter (Draine 2011; see Chapter “The interstellar medium”), i.e. a factor of 10^6 larger. In the IGM, interactions between particles are usually infrequent, and the mean free path of photons is large. As a result, the IGM can be considered nearly transparent (i.e. optically thin) to most types of radiation, and its properties are primarily governed by larger-scale cosmic phenomena rather than local interactions (see Section 2).

Despite its diffuse nature, the IGM plays an important role in cosmology and galaxy evolution. According to the Λ Cold Dark Matter (Λ CDM) paradigm, baryonic matter accounts for $\sim 5\%$ of the total matter-energy content of the Universe, with dark matter comprising about 27%, and dark energy making up the remaining 68% (Planck Collaboration et al. 2020; see Chapters “The expanding Universe” and “The cosmic microwave background”). Out of this $\sim 5\%$ of baryons, the vast majority ($\geq 90\%$) of them are located in the IGM, whereas $\leq 10\%$ are locked up in galaxies or galaxy clusters (Fukugita et al. 1998; Shull et al. 2012; see also Section 3.2). This highlights the fundamental importance of the IGM for studying cosmic structure and baryonic and non-baryonic matter evolution (Hernquist et al. 1996; Croft et al. 1998; Viel et al. 2004; see also Chapter “Cosmology with the Lyman- α forest”). In the early Universe, galaxies formed from the cooling of gas in the IGM that accumulated in dark matter halos (Peebles 1974; Press and Schechter 1974; White and Rees 1978; Mo et al. 2010; see also Chapter “First galaxies”). Since then, the IGM has served as the primary reservoir of gas that continues to feed galaxies, providing the essential material for ongoing star formation, which in turn drives galaxy growth (Tumlinson et al., 2017; Péroux and Howk, 2020). This process is particularly important in the context of galaxy evolution, as the amount of available cold gas in the IGM and CGM directly influences for how long galaxies can sustain star formation (Kereš et al. 2005; Dekel and Birnboim 2006; Faucher-Giguère and Oh 2023; see also Chapter “Cosmological simulations of galaxies”).

1.2 Early discoveries and key observations

The first direct evidence of intervening diffuse matter outside galaxies came right after the discovery of quasars (see Chapter “AGN across cosmic time”) in the 1960’s (Schmidt, 1963). Optical spectroscopy of these bright cosmological sources revealed the presence of intervening metals and neutral hydrogen towards their sightlines, producing absorption lines at redshifts smaller than that of the quasar itself, $z_{\text{abs}} < z_{\text{qso}}$ (Schmidt, 1965; Burbidge et al., 1966; Lynds, 1971). One of the most notable features of these $z \gtrsim 2$ quasar observations is the so-called ‘Lyman- α ($\text{Ly}\alpha$) forest’—a series of packed absorption lines that appear blueward of the quasar’s rest-frame $\text{Ly}\alpha$ emission wavelength ($\lambda_{\text{Ly}\alpha} = 1215.67 \text{ \AA}$) resembling ‘trees’ in a dense forest (see Figure 1; see also Rauch 1998). It was soon recognized that such a signature corresponded to the absorption lines imprinted by a medium containing some amount of neutral hydrogen atoms (H I), located between the quasars and the observer (Bahcall and Salpeter, 1965; Gunn and Peterson, 1965).

Based on the inferred optical depths of these H I absorption lines, Gunn and Peterson (1965) came to an important conclusion: either the space between galaxies was nearly empty or it was highly ionized.¹ Today we know that the correct interpretation is the latter, and these kind of observations allow us to infer that only 1 in every $\sim 10^6$ hydrogen atoms is neutral (see Section 3.2); the IGM is indeed a highly ionized medium (at least at $z \lesssim 6$, i.e. after reionization; see below).

Given its diffuse nature, the IGM does not emit enough photons to allow its detection in emission with current technology (as we usually do with galaxies or other luminous objects). Thus, quasar spectroscopy has remained being the prime technique for probing the IGM *in absorption*. By properly modeling the intervening absorption lines of neutral hydrogen² and other ions (e.g. metals), we can infer the physical properties of the IGM as a function of cosmic time and environment (see Section 3.2). Ultraviolet (UV), optical, and infrared (IR) spectroscopy have been extensively used to probe H I in the late ($z \lesssim 2$), intermediate ($2 \lesssim z \lesssim 5$), and early ($z \gtrsim 5$) Universe, respectively. Over the last decades, these observations, in combination with cosmological hydrodynamical simulations, have brought a

¹Otherwise the expected signal of neutral intervening medium would be that of a quasar continuum completely absorbed blueward to the rest-frame $\text{Ly}\alpha$ emission (see Section 3.2).

²Note that H II ions (free protons) are completely invisible to this technique.

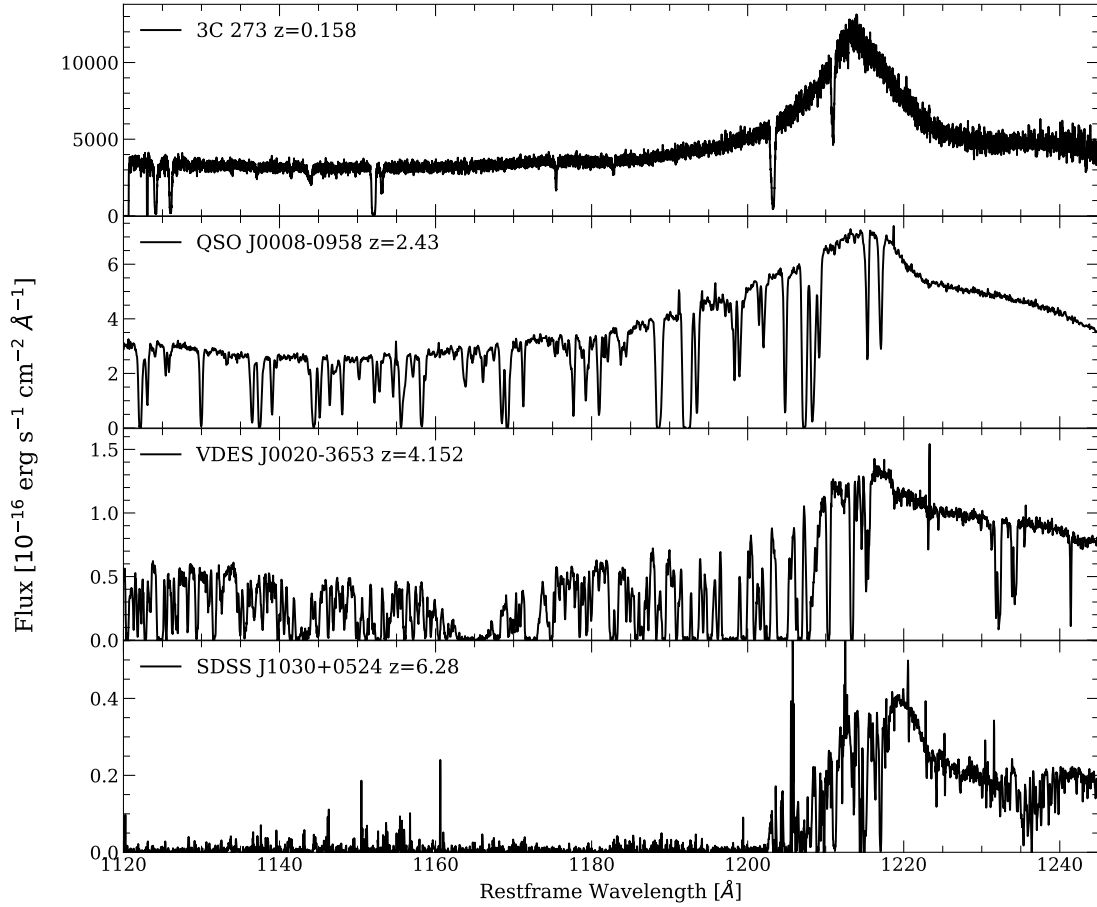


Fig. 1 A sample of quasar spectra covering a wide range redshifts from $0.1 \lesssim z_{\text{qso}} \lesssim 6.3$ (see labels). The wavelength axis is shown in the quasars' rest-frame, such that their $\text{Ly}\alpha$ emission lines are located at $\lambda_{\text{Ly}\alpha}^{\text{qso}} = 1215.67 \text{ \AA}$. The $\text{Ly}\alpha$ -forest towards these quasars is seen as series of absorption lines at wavelengths $\lambda < \lambda_{\text{Ly}\alpha}^{\text{qso}}$. In contrast, at $\lambda > \lambda_{\text{Ly}\alpha}^{\text{qso}}$ the quasar's continuum is mostly unabsorbed (although some metal ion lines are present). This figure illustrates how the $\text{Ly}\alpha$ -forest gets more prominent with redshift, as higher redshift quasars allows us to probe it. Figure credit: K. Martínez-Acosta.

significant advancement of our understanding of the IGM, providing us with a coherent picture of its evolution over cosmic time (McQuinn, 2016).

The main goal of this Chapter is to serve as a first entry point for those interested in studies of the IGM. We provide a general description of the physics of the IGM (Section 2) and an introduction to how we currently observe the IGM with quasar spectroscopy (Section 3). Emphasis is given to the modeling (Section 3.1) and interpretation (Section 3.2) of intervening H I absorption lines, whereas other complementary techniques and future prospects are briefly mentioned (Section 4).

2 The physics of the IGM

2.1 Modeling baryons in a cosmic web shaped by dark matter

Dark matter is the dominant matter component of the Universe that provides the structural skeleton on the largest scales (White and Rees, 1978; Mo et al., 2010). On cosmic (Mpc) scales, dark matter forms a ‘cosmic web’ that extend across the Universe (Bond et al. 1996; see also Chapter “Large-scale structure and the cosmic web”). Baryonic matter is gravitationally attracted to these dark matter structures, accumulating in denser regions, including sheets, filaments and nodes (see Figure 2 and Section 2.4).

At smaller, galaxy halo scales (100 kpc), dark matter’s role becomes particularly important for the formation of stars and galaxies by drawing baryons from the IGM into their very centers. In galaxy formation models, dark matter halos act as sites where baryonic gas can cool and condense to form stars (Press and Schechter 1974; Mo et al. 2010; see also Chapter “Cosmological simulations of galaxies”). Along their evolution, galaxies can expel or recycle their baryons via galactic ‘feedback’ processes—e.g. stellar winds, and active galactic nuclei

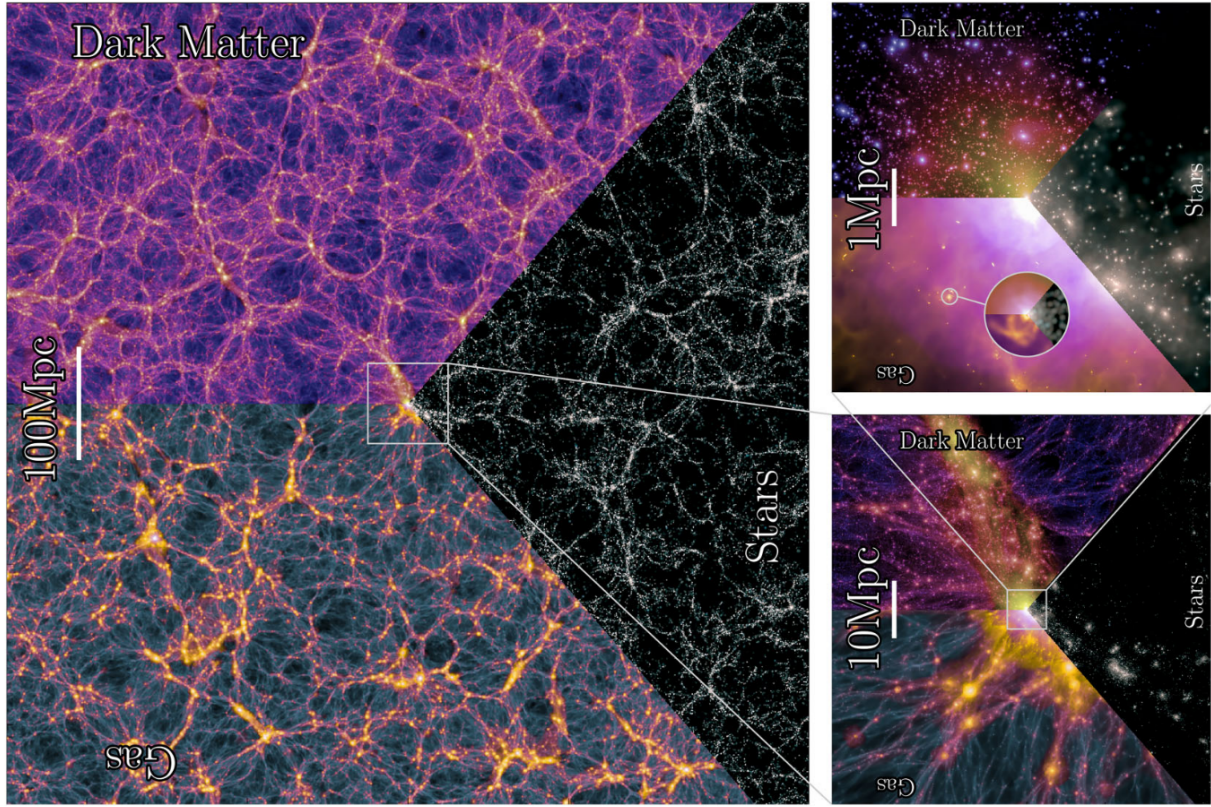


Fig. 2 A visualization of the output of the state-of-the-art cosmological hydrodynamical MillenniumTNG at $z = 0$ (Pakmor et al., 2023). In each sub-panel slices of 10 Mpc in thickness are shown for different components: dark matter (top left), diffuse baryons (gas; bottom left), and stars (right). The left sub-panel covers 740 Mpc on a side, while the insets are a factor of 10 (bottom right) and 100 (top right) smaller. A zoomed in view centred in single galaxy halo (few 100 kpc in diameter) is shown (circles in the top right panel). In the vast volumes of the Universe, diffuse baryons dominate and galaxies (including their stars, planets, dust, etc.) are just extremely small and dense pockets of baryons at the centers of dark matter halos. Yet, galaxies can still influence their surroundings (e.g. the CGM and IGM) via astrophysical processes occurring within them. Figure from Pakmor et al. (2023).

(AGN)—, which heat and enrich their own CGM, and that can also reach the IGM (Veilleux et al. 2020; see also Chapter “Galactic winds and outflows”;). Moreover, high energy photons from hot stars and/or quasars, eventually escape from galaxies injecting further energy into the CGM and IGM (Robertson 2022; see also see Chapter “Reionization and its sources”). These processes change the temperature, ionization state, and chemical composition of the CGM and the IGM, which in turn also influences and affects the future evolution of galaxies (Somerville and Davé, 2015; McQuinn, 2016; Tumlinson et al., 2017; Faucher-Giguère and Oh, 2023).

Despite these complex processes occurring within and near galaxies, the IGM remains relatively simple to model. The key physical ingredients are density, temperature, and ionization state, although metallicity can also be important in some contexts (not extensively discussed here). Therefore, by determining densities as the Universe evolve, and by identifying the main sources of ionization, heating, and cooling, we can, in principle, track the evolution of the physical state of the IGM (Meiksin, 2009; McQuinn, 2016).

2.2 The Epoch of Reionization

The Epoch of Reionization (EoR) is the period in cosmic time where the Universe transitioned from being mostly neutral to being mostly ionized. It is thought that this occurred because high-energy photons produced within the first galaxies (e.g. from young hot stars and/or AGNs) could eventually escape them and started to ionize the hydrogen in the IGM (Robertson 2022; see also Chapter “Reionization and its sources”). Although the exact mechanism(s) of this process is still unknown, observations and current modeling indicate that the EoR lasted between $6 \lesssim z \lesssim 15$; the several transmission spikes observed in the highly absorbed Ly α -forest of $z \sim 6$ quasars are a clear sign that the EoR has already ended at these redshifts (Fan et al. 2006; see also Section 3.2.1). Therefore, the ionization state of the IGM is a function of redshift: before EoR ($z \gtrsim 15$) it was mostly neutral, whereas after EoR ($z \lesssim 6$) it became and stayed a highly ionized medium (McQuinn 2016; see also Section 2.5.1).

2.3 Densities and cosmic environments

The IGM consists of 75% hydrogen and 25% helium, with just traces of heavier elements (Cyburt et al. 2016; see also Chapter “Big Bang Nucleosynthesis”). Initially, the matter distribution was roughly uniform (see Chapter “Linear structure formation”), but as the Universe evolved, the cosmic web structure became more and more complex (see Chapter “Non-linear structure formation”). For tracking densities and environments, it is convenient to define the density contrast, δ , as:

$$\delta \equiv \frac{\rho - \langle \rho \rangle}{\langle \rho \rangle}, \quad (1)$$

where ρ is the actual density at a given location and $\langle \rho \rangle$ is the average density of the Universe. Because the Universe is expanding, δ , ρ and $\langle \rho \rangle$ are function of cosmic time, or redshift, z . In a flat Λ CDM Universe, $\langle \rho \rangle$ is equal to the critical density, ρ_c , which at $z = 0$, corresponds to $\rho_{c,0} \approx 8.6 \times 10^{-30} \text{ g cm}^{-3}$ (Planck Collaboration et al., 2020).³ Therefore, the cosmic baryon density at $z = 0$ corresponds to:

$$\rho_{b,0} = \Omega_{b,0} \rho_{c,0} \approx 4.2 \times 10^{-31} \text{ g cm}^{-3}, \quad (2)$$

where $\Omega_{b,0} \approx 0.05$ is the cosmological baryon density parameter at $z = 0$ (Planck Collaboration et al. 2020; Fields et al. 2020; see also Chapter “Big Bang Nucleosynthesis”). In terms of number density of hydrogen atoms (the dominant baryonic particle in the Universe) this translates to an average of

$$\langle n_H \rangle_0 \approx 2.5 \times 10^{-7} \text{ cm}^{-3}, \quad (3)$$

as mentioned, a million times lower than the typical densities in the ISM. Given that the vast majority of the baryons are in the IGM (see Section 2.4), $\langle n_H \rangle_0$ is comparable to the actual average IGM density. Considering the redshift evolution, we have

$$\langle n_H \rangle = \langle n_H \rangle_0 (1 + z)^3, \quad (4)$$

(similar equations hold for $\langle \rho \rangle$ and $\langle \rho_b \rangle$), i.e. the average number density of hydrogen was larger in the past because the Universe was smaller. For instance, at $z = 3$, $\langle n_H \rangle$ was 64 times larger than $\langle n_H \rangle_0$, i.e. $\langle n_H(z = 3) \rangle = 1.6 \times 10^{-5} \text{ cm}^{-3}$, but this is still a much lower value than the typical ISM densities.⁴

Assuming that baryons follow dark matter (and hence total matter), then

$$\rho_b = \left(\frac{\Omega_b}{\Omega_m} \right) \rho, \quad (5)$$

where $(\Omega_b/\Omega_m) = \text{Const.} \approx 0.17$ is the cosmological ratio of the baryon and matter density parameters (Planck Collaboration et al., 2020), and we can write the density contrast δ in terms of just baryonic densities or just hydrogen number densities, i.e.,

$$\delta = \frac{\rho_b - \langle \rho_b \rangle}{\langle \rho_b \rangle} = \frac{n_H - \langle n_H \rangle}{\langle n_H \rangle}. \quad (6)$$

In this Chapter we will refer to the over/under-density ratio (for $\delta > 0$ and $\delta < 0$, respectively) as,

$$1 + \delta = \frac{\rho}{\langle \rho \rangle} = \frac{\rho}{\rho_c} = \frac{\rho_b}{\langle \rho_b \rangle} = \frac{n_H}{\langle n_H \rangle}. \quad (7)$$

The assumption that baryons follow dark matter in a one-to-one correspondence should only hold in the general case that astrophysical processes (e.g. galaxy feedback) do not severely redistribute baryons. This is certainly not the case in the ISM, while in the CGM at $1 + \delta \gtrsim 200$ (comparable to the virial radii of dark matter halos) this may or may not be true (given the uncertainties in our understanding of galaxy feedback processes; Tumlinson et al. 2017; Amodeo et al. 2021; Faucher-Giguère and Oh 2023). But far away from galaxies at $1 + \delta \lesssim 10 - 20$, this assumption should most likely hold.⁵ These are the relevant overdensity scales for the IGM.

Cosmic environments are defined by topological features like whether matter is distributed in halos (nodes), filaments, sheets, or voids, and studying them is currently a very active area of research (see Chapter “Large-scale structure and the cosmic web”). Clearly, density contrast alone is not sufficient to capture the complexities of the multi-scale network and the non-linear physics involved in the growth of these structures (see Chapter “Non-linear structure formation”). For this reason, in modern astrophysical studies of the IGM (and baryons in general) we depend on hydrodynamical simulations to provide more realistic scenarios to interpret observations.

2.4 Insights from hydrodynamical simulations

2.4.1 Gas phases of diffuse baryons

In contrast to dark matter that only interacts gravitationally, the baryons in the IGM are also affected by pressure (collisions) and radiative processes. The advent of cosmological hydrodynamical simulations since the 1990’s have helped to develop a fairly good understanding

³The critical density of the Universe at $z = 0$ is defined as $\rho_{c,0} \equiv \frac{3H_0^2}{8\pi G}$, where H_0 is the Hubble constant, and G is the gravitational constant.

⁴As an exercise, the reader may compute the redshift where the $\langle n_H \rangle$ was comparable to the typical densities in the ISM.

⁵The very close correspondence between the Λ CDM predictions on these moderate overdensities scales, and the observed properties of the IGM traced by the Ly α -forest (see Section 3.2.3) validates this assumption, at least at $z \gtrsim 2$ (see also Chapter “Cosmology with the Lyman- α forest”).

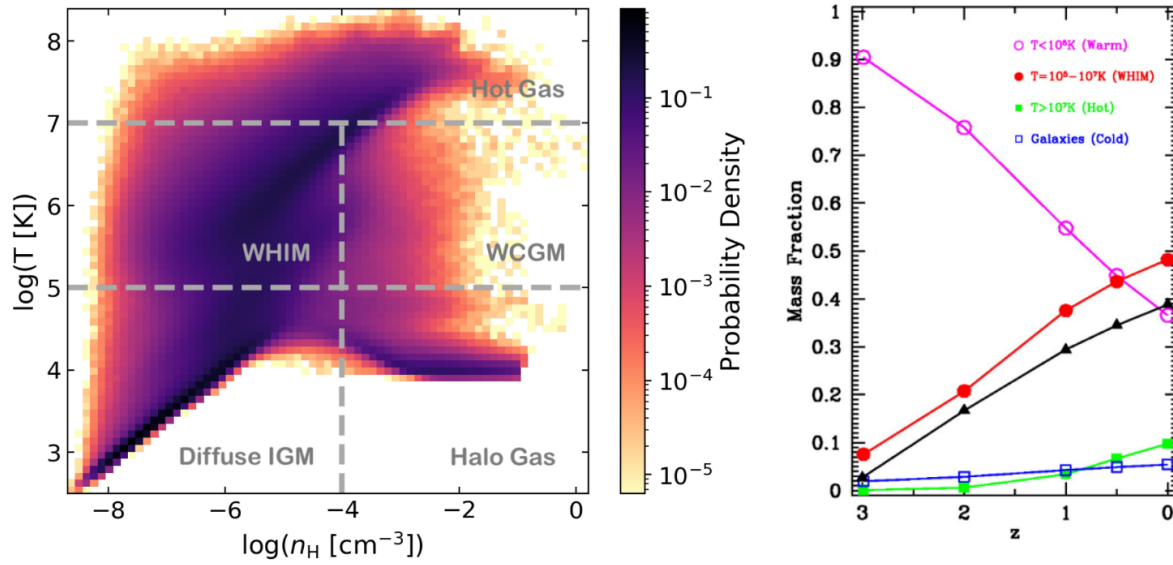


Fig. 3 Left: Density-temperature diagram for diffuse baryons at $z = 0$ from a cosmological hydrodynamical simulation (Illustris TNG; Nelson et al. 2019). The five phases presented in Section 2.4 are labeled. Figure from Galárraga-Espinosa et al. (2021). Right: Mass fractions of the different gas phases as a function of redshift from the hydrodynamical simulation presented by Cen and Ostriker (2006). Although the definition of the gas phases are slightly different than those presented in Section 2.4, this figure illustrates that the diffuse baryons (those outside galaxies) account for $\geq 90\%$ of the baryons in the Universe. At $z \gtrsim 2$, the dominant phase is the diffuse IGM (pink), whereas at $z \lesssim 0.5$ both the diffuse IGM and WHIM (red or black) dominate in almost equal proportion ($\sim 40\%$ each). The exact amount of baryons in the WHIM critically depends on galaxy feedback models. Here, a model with (red) and without (black) galactic winds are shown for reference. Figure adapted from Cen and Ostriker (2006).

and intuition of the key physical processes that govern the different gas phases of the IGM (Cen and Ostriker, 1999; Davé et al., 2001). Despite all the underlying complexity, these simulations indicate that diffuse baryons reside in roughly 5 gas phases based on densities and temperatures (see Figure 3, left panel) defined as follows:

- **Diffuse intergalactic medium (IGM):** at $n_H \lesssim 10^{-4}(1+z) \text{ cm}^{-3}$ and $T < 10^5 \text{ K}$, this phase dominates the baryon budget of the Universe. In terms of overdensities, these correspond to $1 + \delta \lesssim 100$. At these temperatures and densities, this gas is mostly photoheated and photoionized, and a tight correlation between density and temperature arises (see Section 2.5.2). This phase is traced by the Ly α -forest (see Section 3.2.2; see also Rauch 1998).
- **Warm-hot intergalactic medium (WHIM):** at $n_H \lesssim 10^{-4}(1+z) \text{ cm}^{-3}$ and $10^5 \leq T < 10^7 \text{ K}$, this phase builds up in importance as the Universe evolves and the large scale structures become more massive and dense. Most of this gas is shock heated either due to gravitational collapse and/or by galaxy feedback mechanisms, and resides in mild overdensities of $1 \lesssim 1 + \delta \lesssim 100$ close to galaxies (e.g. cosmological filaments connecting galaxy clusters and/or galaxy clusters outskirts). At these temperatures, the gas is mostly collisionally ionized (see Section 2.5.1). This phase has been very challenging to observe directly (see Section 3.2.3).
- **Halo gas (cold):** at $10^{-4}(1+z) \lesssim n_H \lesssim 10^{-1} \text{ cm}^{-3}$ and $T < 10^5 \text{ K}$, this phase corresponds to ‘cool’ gas within galaxy halos, including the CGM or diffuse ISM within galaxies, typically at $T \sim 10^4 \text{ K}$. At densities higher than $\approx 10^{-1} \text{ cm}^{-3}$, the gas is typically associated with star-forming regions in the ISM, and thus not included here (but see Chapters “The interstellar medium” and “Gas in galaxies”). In terms of overdensities, this gas is typically within or around virialized halos at $1 + \delta \gtrsim 200 - 1000$. At these temperatures and densities, it is expected that the gas is mostly photoionized. This phase can be observed either in emission (for the densest parts) and/or in absorption against a background source. Most of the intervening low-ionization metal absorption lines observed towards quasars are tracers of this phase (e.g. Werk et al. 2014; see Chapter “Circumgalactic medium”).
- **Warm circumgalactic medium (WCGM):** at $10^{-4}(1+z) \lesssim n_H \lesssim 10^{-1} \text{ cm}^{-3}$ and $10^5 \leq T < 10^7 \text{ K}$, this phase corresponds to ‘warm’ gas within galaxy halos, typically in the CGM at overdensities $1 + \delta \gtrsim 200 - 1000$. At these temperatures and densities, the gas is likely to be collisionally ionized (see Section 2.5.1). This phase can be observed in emission and/or absorption against a background source. Most of the intervening high-ionization metal absorption lines are likely tracing this phase (e.g. Aracil et al. 2004; Tripp et al. 2008; Burchett et al. 2019; see Chapter “Circumgalactic medium”).
- **Hot gas:** at $T > 10^7 \text{ K}$ (regardless of density) this gas is tracing a ‘hot’ medium, with temperatures comparable or larger than the virial temperature of massive galaxy clusters. This gas is mostly shock-heated and collisionally ionized. This phase can be observed in X-ray emission via Bremsstrahlung radiation (free-free emission) and highly ionized line emission, e.g. in the intracluster medium (see Chapter “Galaxy clusters and the local Universe”).

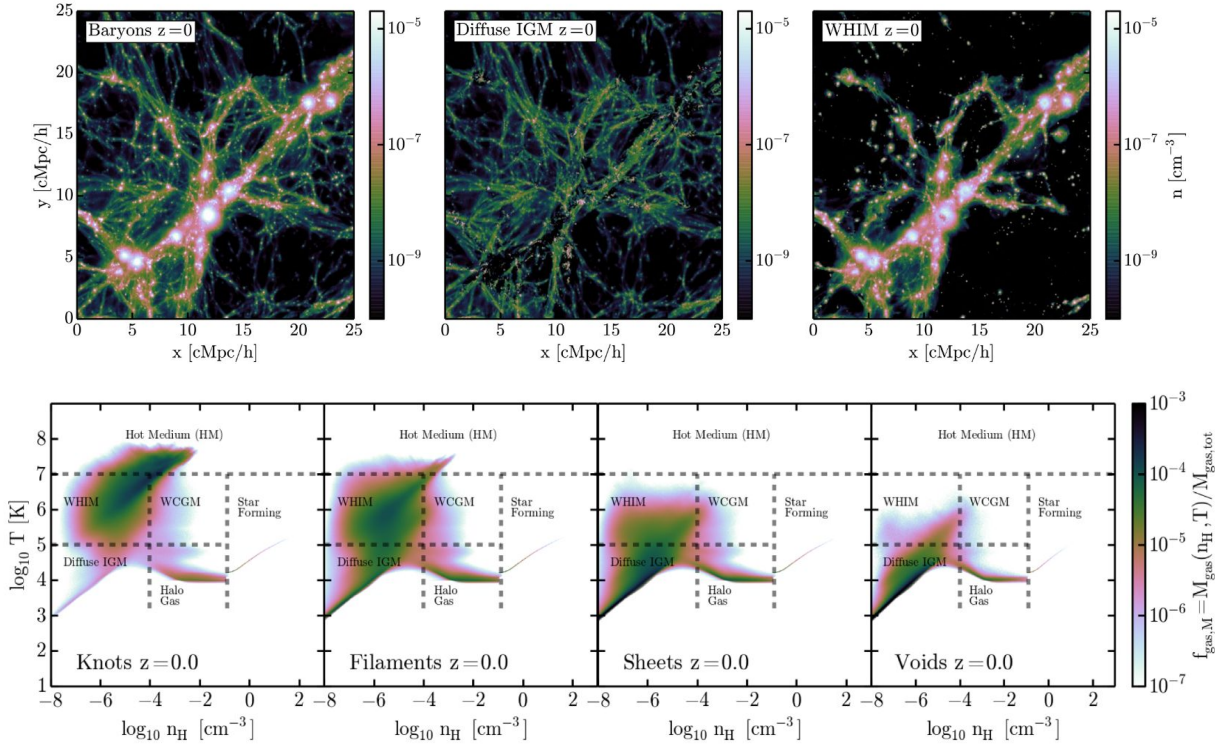


Fig. 4 Top: The $z = 0$ distribution of all baryons (left), baryons in the diffuse IGM (middle) and baryons in the WHIM (right), over tens of co-moving Mpc (cMpc) from a state-of-the-art cosmological hydrodynamical simulation as presented by Martizzi et al. (2019). The color bar represents density. Bottom: The density-temperature diagram for different cosmic environments (from left to right): knots, filaments, sheets and voids. The color bar represents total gas mass fractions. This figure illustrates that the diffuse IGM is mostly located in voids, sheets and filaments, while the WHIM is mostly found in knots and dense filaments, usually connecting galaxy clusters. Figure adapted from Martizzi et al. (2019).

The exact density threshold adopted to divide these phases varies between different researchers and/or simulations, but it broadly corresponds to the IGM/CGM transition at the outskirts of virialized structures (galaxy halos). This limit can also vary as a function of redshift: for instance, the quoted value of $10^{-4}(1+z)\text{cm}^{-3}$ is the one used by Martizzi et al. (2019), which captures this transition sufficiently well across various cosmic epochs for their analyzed simulation (but see Davé et al. 2010 for a different one). Similarly, star-formation requires a minimum density, and the limit of 0.13cm^{-3} (or similar) is adopted as the interface between the diffuse medium and the star-forming gas (e.g. within the ISM). On the other hand, the temperature threshold at $T = 10^5\text{K}$ corresponds to the temperature where collisional ionization starts to become important for hydrogen (see Section 2.5.1), and is used by most researchers. Finally, the inclusion of the ‘hot gas’ as a separate phase is not universally adopted, and some researchers divide these diffuse baryons just into the other four phases.

2.4.2 Baryon budget and redshift evolution

Out of these different phases, the diffuse IGM largely dominates the baryon budget at $z \gtrsim 2$, whereas at $z \lesssim 0.5$ both the WHIM and diffuse IGM become almost equally important (see Figure 3, right panels). The diffuse IGM and the WHIM are the primary focus of this Chapter. We refer the reader to Chapters “Circumgalactic medium”, “Gas in galaxies” and “Galaxy clusters and the local Universe” (and references therein) for more details on the other three phases.

Baryons can transit from one phase to another as a function of time as the Universe expands, cosmic structures grow, and galaxies evolve. Early studies from hydrodynamical simulations predicted the existence of a significant fraction ($\gtrsim 40 - 50\%$) of baryons in the WHIM residing in large and dense cosmological filaments at $z \lesssim 0.5$ (Cen and Ostriker, 1999; Davé et al., 2001). This WHIM has been very elusive to observe (Bregman, 2007; Shull et al., 2012) but is currently our best candidate to host the so-called ‘missing baryons’ (Fukugita et al., 1998). At any given time, the relative importance of each phase also depends on the environment: theoretical studies have established that the diffuse IGM is mostly located in voids, sheets and filaments, while the WHIM is mostly found in dense filaments and knots (e.g. Martizzi et al. 2019; see Figure 4).

Hydrodynamical simulations provide important insights regarding the complexities of the IGM in different environments, but let us come back to more basic physical principles that will allow us to model observations of the IGM.

2.5 Modeling ionization and thermal state

Both the ionization and thermal state of the IGM are regulated by the radiative and collisional processes that affect a gaseous medium. In particular, the properties of the IGM are influenced by processes such as: cosmic expansion, gravitational collapse, shock heating from large-scale structure formation, and energy input from quasars, hot stars, and supernovae.

2.5.1 Ionization state

The ionization state of a medium reflects the balance between ionizing sources and recombination processes. The IGM is predominantly ionized due to high-energy photons from quasars and star-forming galaxies that contribute to a UV background (UVB) radiation that permeates the Universe's volume. In this Section we will present an overview of the dominant mechanisms for determining the ionization state of the IGM, including photoionization, collisional ionization, radiative recombination, and ionization equilibrium.

Photoionization

Let us consider a gas composed of hydrogen atoms. If this gas is receiving incident radiation of sufficient energy, then the neutral atoms (H^0 , also referred to as H I) will interact with it and can become photoionized, by losing an electron:

$$H^0 + h\nu \rightarrow H^+ + e^-, \quad (8)$$

where H^+ represents ionized hydrogen (i.e. a free proton, also referred to as H II), h is the Planck constant, ν is the photon frequency, and e^- represents a free electron. The rate at which H II ions are produced by photoionization is:

$$\frac{dn_{\text{HII}}}{dt} = n_{\text{HI}} n_\gamma \sigma_{\text{p.i.}} c, \quad (9)$$

where n_{HI} is the number density of neutral hydrogen, n_γ is the number density of photons, $\sigma_{\text{p.i.}}$ is the cross-section for photoionization, and c is the speed of light. A good approximation of the $\sigma_{\text{p.i.}}$ for $h\nu > 13.6 \text{ eV}$ is given by Draine (2011):

$$\sigma_{\text{p.i.}} \approx 0.225 a_0^2 \left(\frac{h\nu}{13.6 \text{ eV}} \right)^{-3} \quad (10)$$

$$\approx 6.30 \times 10^{-18} \text{ cm}^2 \left(\frac{h\nu}{13.6 \text{ eV}} \right)^{-3}, \quad (11)$$

with a_0 being the Bohr radius. The rapid decrease of $\sigma_{\text{p.i.}}$ with frequency indicates that photons with energies just above 13.6 eV are the dominant ones in this process. Finally, the photoionization rate is defined as

$$\Gamma_{\text{HI}} \equiv \int_{\nu_{\text{th}}}^{\infty} n_\gamma \sigma_{\text{p.i.}} c \, d\nu = \int_{\nu_{\text{th}}}^{\infty} \frac{u(\nu)}{h\nu} \sigma_{\text{p.i.}} c \, d\nu, \quad (12)$$

where ν_{th} is the photon frequency threshold that can ionize H I ($\nu_{\text{th}} = 13.6 \text{ eV}/h = 3.2 \times 10^{15} \text{ Hz}$, corresponding to a wavelength of 912 Å), and $u(\nu)$ is the specific energy density of the radiation field ($n_\gamma = \frac{u(\nu)}{h\nu}$), such that Equation 9 can be written as:

$$\frac{dn_{\text{HII}}}{dt} = n_{\text{HI}} \Gamma_{\text{HI}}. \quad (13)$$

The photoionization rate corresponds to the rate at which a single neutral hydrogen atom is ionized, usually expressed in units of s^{-1} . Because the IGM is a highly ionized optically thin medium, these high-energy photons (after escaping their original galaxies) travel freely contributing to the UVB responsible for maintaining such an ionization state. Figure 5 shows models and observational constraints of Γ_{HI} as a function of redshift. Estimated values for Γ_{HI} from the UVB range between $\Gamma_{\text{HI}} \sim 10^{-12} \text{ s}^{-1}$ at $z > 2$ and $\Gamma_{\text{HI}} \sim 1 - 10 \times 10^{-14} \text{ s}^{-1}$ at $z \sim 0$ (e.g. Haardt and Madau 2012; Khaire and Srianand 2019). The photoionization timescale, defined as $t_{\text{p.i.}} \sim \frac{1}{\Gamma_{\text{HI}}}$, is then $\sim 40\,000 \text{ yr}$ at $z = 2 - 5$ and $\sim 0.4 - 4 \text{ Myr}$ at $z \lesssim 0.5$.

Collisional ionization

If the temperatures of the gas is sufficiently high, then interactions with free electrons can also collisionally ionized the neutral atoms:

$$H^0 + e^- \rightarrow H^+ + 2e^-, \quad (14)$$

and the rate at which ions H^+ are produced by collisional ionization is:

$$\frac{dn_{\text{HII}}}{dt} = n_{\text{HI}} n_e \langle \sigma_{\text{c.i.}} v \rangle, \quad (15)$$

where n_e is the number density of free electrons, $\sigma_{\text{c.i.}}$ is the cross-section for collisional ionization, and v is the relative speed of free electrons with respect to the neutral hydrogen atoms. Given that electrons are much lighter than H I atoms, v can be approximated by the electron speeds. The term $\langle \sigma_{\text{c.i.}} v \rangle$ represents the average product of $\sigma_{\text{c.i.}}$ and v over the distribution of speeds (or energies) given by the gas temperature T . Usually, this $\langle \sigma_{\text{c.i.}} v \rangle$ term is referred to as the collisional ionization rate coefficient, $k_{\text{c.i.}}(T)$, such that Equation 15 can be

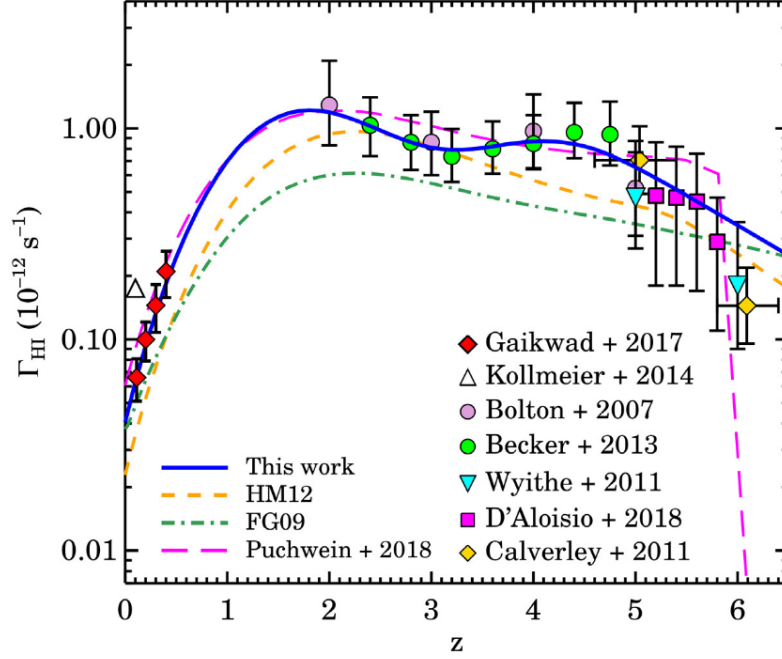


Fig. 5 Models and observational constraints for the IGM photoionization rates from the UVB (Γ_{HI}) as a function of redshift. The models from Khaire and Srianand (2019) (blue-solid line) and from Haardt and Madau (2012) (yellow-dashed line), among others (see references in Khaire and Srianand 2019), are shown. Figure from Khaire and Srianand (2019).

written as:

$$\frac{dn_{\text{HII}}}{dt} = n_{\text{HI}} n_e k_{\text{c.i.}}(T), \quad (16)$$

Assuming kinetic equilibrium, $k_{\text{c.i.}}(T)$, can be computed from a Maxwellian distribution of energies (given the speeds) as,

$$k_{\text{c.i.}}(T) = \left(\frac{8kT}{\pi m_e}\right)^{1/2} \int_{I_H}^{\infty} \sigma_{\text{c.i.}} \frac{E}{kT} \exp\left(-\frac{E}{kT}\right) \frac{dE}{kT}, \quad (17)$$

where m_e is the electron mass, k is the Boltzmann constant, and I_H is the energy threshold for ionizing H I ($I_H = 13.6 \text{ eV}$). The precise values for $\sigma_{\text{c.i.}}$ are determined from experiments, but a useful approximation for energies $E > I_H$ is given by (Draine, 2011):

$$\sigma_{\text{c.i.}} \approx 1.07 \pi a_0^2 \left(1 - \frac{I_H}{E}\right), \quad (18)$$

from which Equation 17 yields,

$$k_{\text{c.i.}}(T) \approx 1.07 \pi a_0^2 \left(\frac{8kT}{\pi m_e}\right)^{1/2} \exp\left(-\frac{I_H}{kT}\right) \quad (19)$$

$$\approx 5.85 \times 10^{-9} \text{ cm}^3 \text{ s}^{-1} \left(\frac{T}{10^4 \text{ K}}\right)^{1/2} \exp\left(-\frac{I_H}{kT}\right). \quad (20)$$

The exponential cut-off of $k_{\text{c.i.}}$ at low kinetic energies, imply that collisional ionization is negligible at temperatures $T \ll I_H/k = 1.58 \times 10^5 \text{ K}$, as expected. Therefore, for applications within the context of the diffuse IGM this mechanisms can be ignored, but it is highly relevant for the WHIM.

Radiative recombination

The opposite process to ionization is recombination. In the case of radiative recombination, the ionized hydrogen captures a free electron and a photon is emitted:



The rate at which H I atoms are produced in this case is:

$$\frac{dn_{\text{HI}}}{dt} = n_{\text{HII}} n_e \langle \sigma_{\text{r.r.}} v \rangle, \quad (22)$$

where n_{HII} is the number density of ionized hydrogen, n_e is the number density of free electrons, $\sigma_{\text{r.r.}}$ is the cross-section for the radiative recombination, and v is the relative speed of free electrons with respect to the ionized hydrogen. Again, given that electrons are much lighter than protons, v can be approximated by the electron speeds. Similarly to the collisional ionization case, the term $\langle \sigma_{\text{r.r.}} v \rangle$ represents the average product of $\sigma_{\text{r.r.}}$ and v over the distribution of speeds (or energies) given by the gas temperature T , and is usually referred to as the radiative recombination rate coefficient, $\alpha(T)$. With this notation, Equation 22 can be written as:

$$\frac{dn_{\text{HI}}}{dt} = n_{\text{HII}} n_e \alpha(T). \quad (23)$$

Again, assuming kinetic equilibrium, $\alpha(T)$, can also be computed from a Maxwellian distribution of energies, but we need to consider all possible quantum numbers (n, l) of the hydrogen atom to which electrons can be recombined. For a particular quantum number, we have:

$$\alpha_{nl}(T) = \left(\frac{8kT}{\pi m_e} \right)^{1/2} \int_0^\infty \sigma_{\text{r.r.},nl} \frac{E}{kT} \exp\left(-\frac{E}{kT}\right) \frac{dE}{kT}, \quad (24)$$

and the effective $\alpha(T)$ is obtained by summing over all possible quantum numbers. As pointed out by Baker and Menzel (1938), two extreme cases could be considered: i) an optically thin cloud where all photons produced by recombination escape the system (Case A), and ii) an optically thick cloud where photons produced by recombination to the ground level ($n = 1$) cannot escape because these are immediately reabsorbed (Case B). Thus we have:

$$\alpha_A(T) = \sum_{n=1}^\infty \sum_{l=0}^{n-1} \alpha_{nl}(T), \quad (25)$$

$$\alpha_B(T) = \sum_{n=2}^\infty \sum_{l=0}^{n-1} \alpha_{nl}(T) = \alpha_A(T) - \alpha_{1s}(T), \quad (26)$$

respectively. The exact values are determined by quantum mechanics and/or experiments, but these two cases can be approximated by (Draine, 2011):

$$\alpha_A(T) \approx 4.13 \times 10^{-13} \text{ cm}^3 \text{ s}^{-1} \left(\frac{T}{10^4 \text{ K}} \right)^{-0.71}, \quad (27)$$

$$\alpha_B(T) \approx 2.54 \times 10^{-13} \text{ cm}^3 \text{ s}^{-1} \left(\frac{T}{10^4 \text{ K}} \right)^{-0.81}, \quad (28)$$

respectively. For applications regarding the IGM, we will be mostly concerned with Case A. The radiative recombination timescale is defined as $t_{\text{r.r.}} \sim \frac{1}{n_e \alpha(T)}$, and thus depends on both density of free electrons and temperature. For the IGM, and parametrizing the electron density in terms of the mean density of the Universe, this corresponds to,

$$t_{\text{r.r.}} \approx 9.7 \times 10^{18} \text{ s} \frac{\langle n_{\text{H}} \rangle_0 (1+z)^{-3}}{n_e} \left(\frac{T}{10^4 \text{ K}} \right)^{0.71}, \quad (29)$$

implying that for highly ionized gas at mean density, $t_{\text{r.r.}} \gg t_{\text{p,i}}$ at $z = 0 - 6$. This explains why after reionization, most of the IGM remains highly ionized.

Ionization equilibrium and ionization fractions

A particularly interesting case is that of ionization equilibrium, in which the rates at which H I are converted into H II, and vice-versa, are equal:

$$\frac{dn_{\text{HII}}}{dt} = \frac{dn_{\text{HI}}}{dt} \quad (30)$$

$$n_{\text{HI}} \Gamma_{\text{HI}} + n_{\text{HI}} n_{\text{HII}} k_{\text{c.i.}}(T) = n_{\text{HII}}^2 \alpha(T) \quad (31)$$

considering that $n_e = n_{\text{HII}}$ for an overall neutral plasma. Let us define the neutral and ionized gas fractions as

$$x_{\text{HI}} \equiv \frac{n_{\text{HI}}}{n_{\text{H}}} = \frac{n_{\text{HI}}}{n_{\text{HI}} + n_{\text{HII}}}, \quad (32)$$

$$x_{\text{HII}} \equiv \frac{n_{\text{HII}}}{n_{\text{H}}} = \frac{n_{\text{HII}}}{n_{\text{HI}} + n_{\text{HII}}}, \quad (33)$$

respectively. Then, $n_{\text{HII}} = x_{\text{HII}} n_{\text{H}}$ and $n_{\text{HI}} = x_{\text{HI}} n_{\text{H}} = (1 - x_{\text{HII}}) n_{\text{H}}$. We can write Equation 31 as a quadratic equation for x_{HII} as:

$$x_{\text{HII}}^2 n_{\text{H}} \{\alpha(T) + k_{\text{c.i.}}(T)\} + x_{\text{HII}} \{\Gamma_{\text{HI}} - n_{\text{H}} k_{\text{c.i.}}(T)\} - \Gamma_{\text{HI}} = 0. \quad (34)$$

Solving this equation for a given n_H , $\alpha(T)$, Γ_{HI} and $k_{\text{c.i.}}(T)$ provides the ionized fraction x_{HII} (and hence the neutral fraction $x_{\text{HI}} = 1 - x_{\text{HII}}$) of the gas. However, this solution is not necessarily straightforward, as it requires the knowledge of the thermal state (T) and shape and intensity of the radiation field encoded in Γ_{HI} for a given n_H . We note here that the thermal state of the gas is critically regulated by the amount of metal ions via radiative cooling and thus the metallicity of the gas is an important parameter to consider, especially in high density regions close to galaxies (see Section 2.5.2). Similarly, the sources and the interaction of the radiation field with the gas itself is also important (especially in dense environments), where radiative transfer equations must be explicitly solved for a given geometry. The inclusion of all these effects makes this problem sufficiently complex that dedicated software and/or the use of hydrodynamical simulations are required. For instance, the code `CLOUDY` (Ferland et al., 1998) is widely used to infer the underlying physical conditions of the gas in widely diverse gaseous astrophysical environments. Although most complications arise in dense environments close to or within galaxies, some limiting cases can become good approximations in practice:

- **Photoionization equilibrium (PIE):** Assuming temperatures sufficiently low that $k_{\text{c.i.}}$ can be ignored ($T < 10^5$ K; see Equation 20), then Equation 34 is approximated to:

$$x_{\text{HII}}^2 \frac{n_H \alpha(T)}{\Gamma_{\text{HI}}} + x_{\text{HII}} - 1 \approx 0, \quad (35)$$

which can be easily solved.⁶ Here, let us consider two limits based on comparing n_H with the ratio $\Gamma_{\text{HI}}/\alpha(T)$. When $n_H \ll \Gamma_{\text{HI}}/\alpha(T)$ (sufficiently low density environments) then,

$$x_{\text{HII}} \approx 1 - n_H \alpha(T) / \Gamma_{\text{HI}}, \quad (36)$$

implying a neutral fraction of

$$x_{\text{HI}} \approx n_H \alpha(T) / \Gamma_{\text{HI}}. \quad (37)$$

In the case of the IGM at $T \sim 10^4$ K, $\Gamma_{\text{HI}}/\alpha(T) \approx 0.2 - 2 \text{ cm}^{-3}$ (depending on redshift) and $n_H \lesssim 10^{-4} \text{ cm}^{-3}$, and thus Equations 36 and 37 are actually very good approximations. On the other hand, for the case $n_H \gg \Gamma_{\text{HI}}/\alpha(T)$ (sufficiently high density environments) then,

$$x_{\text{HII}} \approx \sqrt{\Gamma_{\text{HI}} / n_H \alpha(T)}, \quad (38)$$

$$x_{\text{HI}} \approx 1 - \sqrt{\Gamma_{\text{HI}} / n_H \alpha(T)}, \quad (39)$$

which are more appropriate for some ISM and/or some CGM environments.

- **Collisional ionization equilibrium (CIE):** Assuming temperatures sufficiently high that collisional ionization dominates ($T > 10^5$ K) and that Γ_{HI} can be ignored, then Equation 34 implies that the ionized and neutral fractions become independent of density and are only functions of temperature,

$$x_{\text{HII}} \approx \frac{k_{\text{c.i.}}(T)}{\alpha(T) + k_{\text{c.i.}}(T)}, \quad (40)$$

$$x_{\text{HI}} \approx \frac{\alpha(T)}{\alpha(T) + k_{\text{c.i.}}(T)}. \quad (41)$$

This approximation is relevant for the WHIM, WCGM and hot gas environments.

2.5.2 Thermal state

The thermal state of the IGM is also regulated by collisional and radiative processes, and is usually estimated by balancing the heating and cooling rates in the context of an expanding Universe. In this Section, we will describe the most important mechanisms and modeling for determining the thermal state of the IGM.

Heating mechanisms

The primary sources of heating in the IGM are:

- **Photoheating:** produced by photons that can ionize either hydrogen or helium. Once an atom of hydrogen or helium is ionized, the free electron(s) produced by the interaction (e.g. Equation 8) carry part of the incident photon energy as kinetic energy. Collisions between these free electrons and the rest of ions heat the medium. Only photons with $E > h\nu_{\text{th}}^{\text{HI}} = 13.6 \text{ eV}$ can ionize hydrogen, whereas for partially or for fully ionizing helium, photons with $E > h\nu_{\text{th}}^{\text{HeI}} = 24.6 \text{ eV}$ and $E > h\nu_{\text{th}}^{\text{HeII}} = 54.4 \text{ eV}$ are required, respectively. The photoheating rate is then:

$$\mathcal{H}_{\text{photo}} = n_{\text{HI}} \int_{\nu_{\text{th}}^{\text{HI}}}^{\infty} \frac{u(\nu)}{h\nu} \sigma_{\text{p.i.}}^{\text{HI}} c (h\nu - h\nu_{\text{th}}^{\text{HI}}) d\nu + n_{\text{HeI}} \int_{\nu_{\text{th}}^{\text{HeI}}}^{\infty} \frac{u(\nu)}{h\nu} \sigma_{\text{p.i.}}^{\text{HeI}} c (h\nu - h\nu_{\text{th}}^{\text{HeI}}) d\nu + n_{\text{HeII}} \int_{\nu_{\text{th}}^{\text{HeII}}}^{\infty} \frac{u(\nu)}{h\nu} \sigma_{\text{p.i.}}^{\text{HeII}} c (h\nu - h\nu_{\text{th}}^{\text{HeII}}) d\nu, \quad (42)$$

where n_{HI} , n_{HeI} and n_{HeII} are the corresponding densities, and $\sigma_{\text{p.i.}}^{\text{HI}}$, $\sigma_{\text{p.i.}}^{\text{HeI}}$, $\sigma_{\text{p.i.}}^{\text{HeII}}$ are the corresponding photoionization cross-sections. The sources of these ionizing photons (i.e. the $u(\nu)$ radiation field) are thought to be produced within galaxies, either from young massive

⁶For a positive solution we have, $x_{\text{HII}} = \frac{-1 + \sqrt{1 + 4a}}{2a}$, with $a \equiv n_H \alpha(T) / \Gamma_{\text{HI}}$.

stars (dominating at early cosmic times) and/or quasars (dominating at late cosmic times and at $E > 54.4$ eV); however, the mechanism that allows these high-energy photons escape the galaxies remains quite uncertain.⁷

- **Adiabatic heating:** produced by the accretion and collapse of matter due to gravity. As baryons fall into the potential wells of overdense structures (e.g. sheets, filaments, nodes or halos) they gain kinetic energy adiabatically.⁸
- **Shock heating from structure formation:** also produced by the accretion and collapse of matter due to gravity. In contrast to adiabatic heating, here the kinetic energy is added via shocks. When accretion speeds are larger than the sound speed of the medium, then a shock front is produced and the gas is suddenly heated due to compression. Shock heating is responsible for the majority of the gas in the WHIM and the hot gas phases of IGM, especially within large and dense cosmological filaments and galaxy clusters (e.g. the ICM).
- **Shock heating from galaxy feedback processes:** produced by energetic outflows from galaxies, driven primarily by stellar winds and supernovae (SNe) from star-forming regions and/or AGN activity. These feedback processes can eject large amounts of gas at high velocities (depending on the models), creating localized shocks as the outflows collide with the surrounding IGM. These shocks can heat the gas to $T > 10^5$ K thus redistributing baryons to the WHIM, warm CGM and hot gas phases. However, the actual relative importance of this process is not well established, as it critically depends on the treatment and modeling used in simulations for star-formation and AGN, often done at the sub-grid level (unresolved; see Somerville and Davé 2015 for a review).

Cooling mechanisms

The primary mechanisms of cooling the gas in the IGM are:

- **Adiabatic cooling:** produced by the expansion of the Universe. As the density of non-virialized structures decreases, baryons lose kinetic energy adiabatically.⁸ This mechanism is particularly important after EoR and dominates the cooling of the IGM at $z \lesssim 6$.
- **Compton cooling:** produced by free electrons that interact with lower-energy photons in the medium via scattering. This interaction transfers energy from the electrons to the photons, effectively cooling the medium. In the IGM, these low-energy photons are from the cosmic microwave background CMB), and thus the Compton cooling rate is (Weymann, 1965),

$$\Lambda_{\text{Compt.}} = 4n_e c \frac{\sigma_T}{m_e c^2} a_{\text{rad}} T_{\text{CMB}}^4(z) k(T - T_{\text{CMB}}(z)), \quad (43)$$

where σ_T is the Thomson cross-section, a_{rad} is the radiation density constant, and $T_{\text{CMB}}(z) = T_{\text{CMB},0}(1+z)$ is the temperature of the CMB as a function of z , with $T_{\text{CMB},0} \approx 2.7$ K. Compton cooling is more relevant for gas at $T \gtrsim 10^7$ K, and also particularly important at $z \gtrsim 6$, i.e. before EoR (see Chapter “Reionization and its sources”).

- **Collisional excitation cooling:** produced by free electrons that collide with ions and have enough energy to excite them. Once the ions return to their ground state by emitting photons, these carry energy away from the medium, thus cooling the gas. This process is more relevant for enriched gas at $10^4 < T \lesssim 10^6$ K.
- **Collisional ionization cooling:** produced by free electrons that collide with ions and have enough energy to ionize them. The energy required to ionize the ions is effectively taken from the kinetic energy of the colliding electrons, thus cooling the gas. This process is more relevant for enriched gas at $T > 10^5$ K.
- **Radiative recombination cooling:** produced by free electrons that recombine into ions. The emitted photons in the process (Equation 21), carry energy away from the medium, thus cooling the gas. This process is more relevant for enriched gas at $10^4 < T \lesssim 10^5$ K.
- **Bremsstrahlung (free-free emission) cooling:** produced by free electrons when these are deflected by charged ions (typically protons). Due to the acceleration of the electrons, photons are emitted which carry energy away from the medium. At the densities considered here, this process is more relevant for gas at $10^6 < T \lesssim 10^8$ K, e.g. in galaxy clusters or massive groups (see Chapter “Galaxy clusters and the local Universe”).

Although in this Chapter we have mostly focused in hydrogen and helium, here it is important to emphasize that for collisional and radiative recombination cooling, the metallicity of the gas must be critically taken into account (specially in the densest and more enriched gas phases, like the CGM; see Chapter “Circumgalactic medium”). Metal ions provide additional energy levels and transitions that allow the gas to lose energy more efficiently, especially at $10^5 \lesssim T \lesssim 10^7$ K where hydrogen and helium alone are not quite effective coolants (e.g. Wiersma et al., 2009).

Modeling the thermal evolution of the IGM

The temperature evolution of the IGM is modeled as (Hui and Gnedin, 1997; Upton Sanderbeck et al., 2016),

$$\frac{dT}{dt} = -2HT + \frac{2}{3} \frac{T}{(1+\delta)} \frac{d\delta}{dt} - \frac{T}{n_{\text{tot}}} \frac{dn_{\text{tot}}}{dt} + \frac{2}{3kn_{\text{tot}}} \frac{dQ}{dt}, \quad (44)$$

⁷Note that high-energy photons ($E > 13.6$ eV) have large cross-sections (Equation 11) and thus are likely to be absorbed by the surrounding gas and thus remain within the galaxies. Similarly, interaction of these photons with dust grains in the ISM also prevent them from easily escaping.

⁸This process is a consequence of the first law of thermodynamics which states that, in the absence of heat exchange with the surroundings, the compression/expansion of the system will lead to an increase/decrease in temperature.

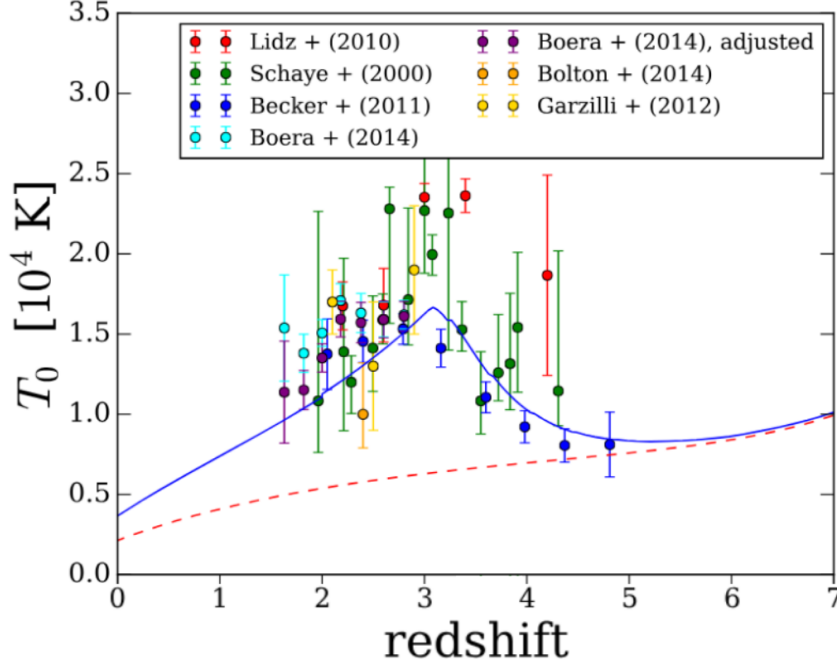


Fig. 6 Models and observations for the temperature of the IGM at mean density, T_0 , as a function of redshift. Two models from Upton Sanderbeck et al. (2016) are shown: with (blue-solid line) and without (red-dashed line) He II reionization. Observational constraints from several studies are also shown (see compilation by Upton Sanderbeck et al. 2016). Figure adapted from Upton Sanderbeck et al. (2016).

where d/dt is the Lagrangian time derivative, H is the Hubble parameter⁹, δ is the density contrast, n_{tot} is the total number density of free baryonic particles (ions and electrons)¹⁰, k is the Boltzmann constant, and dQ/dt is the heat gain per unit volume. The first two terms correspond to adiabatic cooling and heating, respectively. The third term corresponds to the change of internal energy per particle as the number of particles vary. Typically this term is unimportant ($dn_{\text{tot}}/dt \approx 0$) except right after hydrogen and helium reionization. The fourth term includes all the other sources of heating and cooling previously mentioned, although in most modelings shock heating is treated separately or is not considered.

This modeling has been successful at reproducing observational constraints at $z > 1$ (without shocks). Figure 6 shows two models for the evolution of the temperature of the IGM at mean density, T_0 , as a function of redshift from Upton Sanderbeck et al. (2016): with (blue line) and without (red dashed line) He II reionization. Some measurements from various works using a variety of techniques (see references in Upton Sanderbeck et al. 2016) are also shown for comparison. The temperature of the IGM evolves slowly with redshift, with typical values $T_0 \sim 1 - 2 \times 10^4$ K. The peak of T_0 at $z \sim 3$ favors the interpretation of a late He II reionization. These measurements and modeling also indicate that for the diffuse IGM between $2 \lesssim z \lesssim 6$, photoheating from the UVB is the dominant source of heating, whereas both adiabatic and Compton cooling are the dominant coolants (McQuinn and Upton Sanderbeck, 2016). Therefore, for most applications concerning the diffuse IGM, dQ/dt , can be well approximated as

$$\frac{dQ}{dt} \approx \mathcal{H}_{\text{photo}} - \Lambda_{\text{Compt}}. \quad (45)$$

The density-temperature relation for the diffuse IGM

The diffuse IGM presents an strikingly tight correlation between density and temperature. This behavior is apparent in the temperature-density phase diagram of hydrodynamical simulations, such as those presented in Figures 3 and 4. The previous modeling of the thermal history (Equation 44) have helped to establish the origin of this remarkable feature (Miralda-Escudé and Rees, 1994; Hui and Gnedin, 1997; Theuns et al., 1998). The “observed”¹¹ relation has a power-law form,

$$T \approx T_0(1 + \delta)^{\gamma-1}, \quad (46)$$

with $\gamma > 1$ and where $\gamma - 1 \approx 0.6$. Interestingly, the vast majority of the diffuse IGM is expected to follow this trend, starting right after

⁹For a flat Λ CDM cosmology this is defined as $H \equiv H_0 \sqrt{\Omega_m(1+z)^3 + \Omega_\Lambda}$ where H_0 is the Hubble constant.

¹⁰Despite electrons being leptons, these are usually included as ‘baryons’ by astronomers.

¹¹Observed in hydrodynamical simulations.

re-ionization ends. Given that the photoheating timescales ($t = 1/\Gamma_{\text{HI}}$; see Section 2.5.1) are much shorter than the Hubble times, an equilibrium temperature is rapidly reached for a given density n_{H} (Hui and Gnedin 1997, see also McQuinn and Upton Sanderbeck 2016). Assuming PIE in the low density regime (Equation 37), $n_{\text{H}}\Gamma_{\text{HI}} = n_{\text{H}}^2\alpha(T)$ with $\alpha(T) \propto T^{-\beta}$ (see Section 2.5.1). Parametrizing n_{H} and T as a function of overdensity $(1 + \delta)$, Equation 44 can be solved for a $T(1 + \delta)$. Ignoring non-adiabatic cooling terms, this approach leads to a solution of the form $T = T_0(1 + \delta)^{1/(1+\beta)}$ with $\beta \approx 0.7$ (Case A; see Equation 27), corresponding to $T = T_0(1 + \delta)^{1/1.7} \approx T_0(1 + \delta)^{0.6}$ (Miralda-Escudé and Rees, 1994; Hui and Gnedin, 1997; Theuns et al., 1998). The previous argument indicates that the temperature-density relation arises from the balance between photo-heating and adiabatic cooling. However, McQuinn and Upton Sanderbeck (2016) have argued that the slope is actually set by the fact that the ratio between the photo-heating rate and $n_{\text{H}}^{2/3}$ is almost constant (see their equation 12), whereas adiabatic (and Compton) cooling only help the gas to reach this equilibrium faster.

The previous treatment ignores the effect of shocks in the IGM. At $T \gtrsim 10^5$ K, shock heating and collisions are important and Equation 46 no longer holds. Indeed, shocks will tend to move gas away from any density-temperature relation, and thus these will increase the scatter around it if such a relation exists (McQuinn and Upton Sanderbeck, 2016). Shocks in the IGM become more important as the Universe evolves, especially at $z \lesssim 1$ (see Section 2.4). In the WHIM, shocks produced by structure formation are expected to dominate the heating, but galaxy feedback shocks may also be important (depending on the models). Although a similar temperature-density relation could be seen in the WHIM of some hydrodynamical simulations (e.g. Galárraga-Espinosa et al. 2021; see Figure 3), these are not as tight as the one in the diffuse IGM, and the slope is not set to a universal value (model dependent).

2.6 Hydrodynamical equilibrium in the diffuse IGM

Observations of the IGM are typically achieved via the absorption lines imprinted in the spectra of background quasars, and this technique can only access the neutral hydrogen atoms (see Section 3.2). Thus, it is worthwhile finding an expression for the characteristic neutral hydrogen column density, N_{HI} , for a given n_{H} , T and Γ_{HI} , in this highly ionized medium.

The general properties of the diffuse IGM can be understood based on stability arguments. Assuming IGM “clouds” are self gravitating systems in hydrostatic equilibrium, then the dynamical ($t_{\text{dyn}} \sim 1/\sqrt{\rho G}$) and sound crossing time ($t_{\text{sc}} \sim L/c_s$) should be of the same order, $t_{\text{dyn}} \sim t_{\text{sc}}$ (Schaye, 2001). Here G is the gravitational constant, ρ is the matter density, L is the characteristic size of the cloud, and c_s ($\equiv \sqrt{dP/d\rho}$, where P is the pressure) is the speed of sound within the medium.¹² Accounting for helium abundance, this characteristic size is (Schaye, 2001):

$$L \approx \frac{c_s}{\sqrt{\rho G}} \sim 0.52 \text{ kpc} \left(\frac{n_{\text{H}}}{1 \text{ cm}^{-3}} \right)^{-1/2} \left(\frac{T}{10^4 \text{ K}} \right)^{1/2} \left(\frac{f_g}{0.17} \right)^{1/2}, \quad (47)$$

where f_g is the gas mass fraction. In the context of the IGM, dark matter dominates the matter content and the gas fraction should be $f_g \sim \Omega_b/\Omega_m \approx 0.17$ (Planck Collaboration et al., 2020), while the typical IGM temperature is $T = 10^4$ K. Similarly, one can consider a characteristic column density as (Schaye, 2001):

$$N_{\text{H}} \equiv n_{\text{H}}L \sim 1.6 \times 10^{21} \text{ cm}^{-2} \left(\frac{n_{\text{H}}}{1 \text{ cm}^{-3}} \right)^{1/2} \left(\frac{T}{10^4 \text{ K}} \right)^{1/2} \left(\frac{f_g}{0.17} \right)^{1/2}. \quad (48)$$

For a highly ionized optically thin medium, given the results from Equations 27 and 37 and accounting for helium (Schaye, 2001),

$$N_{\text{HI}} \approx 2.3 \times 10^{13} \text{ cm}^{-2} \left(\frac{n_{\text{H}}}{10^{-5} \text{ cm}^{-3}} \right)^{3/2} \left(\frac{T}{10^4 \text{ K}} \right)^{-0.26} \left(\frac{\Gamma_{\text{HI}}}{10^{-12} \text{ s}^{-1}} \right)^{-1} \left(\frac{f_g}{0.17} \right)^{1/2}, \quad (49)$$

$$N_{\text{HI}} \approx 2.7 \times 10^{13} \text{ cm}^{-2} (1 + \delta)^{3/2} \left(\frac{\Omega_b}{0.05} \right)^{3/2} \left(\frac{1+z}{4} \right)^{9/2} \left(\frac{T}{10^4 \text{ K}} \right)^{-0.26} \left(\frac{\Gamma_{\text{HI}}}{10^{-12} \text{ s}^{-1}} \right)^{-1} \left(\frac{f_g}{0.17} \right)^{1/2}, \quad (50)$$

where the densities have been normalized at $z = 3$ (see Equation 4) and the latter expression is written explicitly in terms of the overdensity $(1 + \delta)$; see Equation 7). This implies that self-gravitating clouds in hydrostatic equilibrium in the IGM at mean cosmological densities and at $T = 10^4$ K would produce absorption lines with neutral hydrogen column densities of $N_{\text{HI}} \sim 3 \times 10^{13} \text{ cm}^{-2}$ at $z = 3$. Increasing/decreasing the temperature has a limited effect given the mild $T^{-0.26}$ dependence. Similarly, increasing/decreasing either the gas fractions or the photoionization rate, also have limited effects given their $1/2$ and -1 exponents. The major dependence’s are for redshift evolution and density contrasts. Rewriting Equation 50 to solve for overdensity we have,

$$(1 + \delta) \approx \left(\frac{N_{\text{HI}}}{10^{13.5} \text{ cm}^{-2}} \right)^{2/3} \left(\frac{\Gamma_{\text{HI}}}{10^{-12} \text{ s}^{-1}} \right)^{2/3} \left(\frac{1+z}{4} \right)^{-3} \left(\frac{T}{10^4 \text{ K}} \right)^{0.17} \left(\frac{f_g}{0.17} \right)^{-1/3} \left(\frac{\Omega_b}{0.05} \right)^{-1}, \quad (51)$$

Equations 49, 50 and 51 are only valid for the diffuse IGM in the mildly overdense cosmic web, at $0 < \delta \lesssim 10$ and at redshifts after reionization at $z < 6$, where the previous assumptions apply. For instance, if we consider a $1 + \delta \approx 10$ at $z = 3$, we expect $N_{\text{HI}} \approx 10^{15} \text{ cm}^{-2}$ (fixing all the rest of the parameters), which is no longer an optically thin cloud (see Section 3.1.2); more complicated ionization corrections are needed that require radiative transfer solvers (e.g. Ferland et al., 1998). However, at $z \approx 0$, an overdensity of $1 + \delta \approx 10$, would correspond to an (almost) optically thin cloud with $N_{\text{HI}} \approx 10^{13.5} \text{ cm}^{-2}$ (even considering $\Gamma_{\text{HI}} \sim 10^{-13} \text{ s}^{-1}$). This illustrates the importance of taking the Universe evolution into account when comparing IGM systems of a given N_{HI} and relating them to overdensities. Finally,

¹²This is the same argument as that applied to the Jeans length.

at sufficiently large column densities $N_{\text{HI}} \gtrsim 10^{19} \text{ cm}^{-2}$, self-shielding will completely protect the inner part of the cloud from the external ionizing UV photons, implying a mostly neutral medium ($n_{\text{HI}} \sim n_{\text{H}}$) and thus, no ionization corrections are needed. In this case, Equation 48 would be a more appropriate approximation, i.e. $N_{\text{HI}} \approx N_{\text{H}}$.

These equations should be considered only as guidelines, and some departures (e.g. the exact normalization and scatter around the relations) are indeed expected. For modeling the WHIM, on the other hand, hydrodynamical simulations are usually required due to the presence of more complex physics, like shocks and instabilities; for instance, Davé et al. (2010) find that at a fixed N_{HI} , WHIM gas is at a $\approx 5 - 10\times$ higher overdensities compared to the diffuse IGM, significantly departing from simply applying Equation 51.

3 Probing the IGM with quasars

3.1 The physics of absorption lines

In this Section we provide an overview of the basic physical principles of absorption lines and how we model them.

3.1.1 Emission and absorption lines

When electromagnetic radiation interacts with ions, there will be physical processes that can produce what we call emission and absorption lines. These are produced at very specific energies, given by quantum mechanics, which translates to specific frequencies or wavelengths in a spectrum. The physical systems that produce emission or absorption lines are usually referred to as ‘emitters’ and ‘absorbers’, respectively. These can be individual ions, or, more typically, ensembles of them (e.g. “clouds” of gas or plasma).

Let us consider a cloud of ions X that has two quantized energy levels: an upper level with energy E_u , and a lower level with energy E_l . If photons of frequencies $\nu_{ul} = (E_u - E_l)/h$ are present, then these can be absorbed by the ions in the lower energy level, X_l , and produce ions excited to the upper level, X_u :

$$X_l + h\nu_{ul} \rightarrow X_u. \quad (52)$$

This process is called “absorption”, and the rate at which this happens is proportional to the number density of X_l ions, n_l , and the specific energy density, u_ν :

$$\left(\frac{dn_u}{dt} \right)_{l \rightarrow u} = - \left(\frac{dn_l}{dt} \right)_{l \rightarrow u} = n_l B_{lu} u_\nu, \quad (53)$$

where the constant of proportionality, B_{lu} is the Einstein B coefficient for this particular transition from X_l to X_u .

In contrast to absorption, “emission” is produced when the X_u ions gets de-excited from the upper to the lower level, by emitting a photon with frequencies $\nu_{ul} = (E_u - E_l)/h$. There are two ways in which process can happen: spontaneous emission and stimulated emission,

$$X_u \rightarrow X_l + h\nu_{ul}, \quad (54)$$

$$X_u + h\nu_{ul} \rightarrow X_l + 2h\nu_{ul}, \quad (55)$$

respectively. As its name suggests, spontaneous emission is independent of the incident radiation field, and its rate is simply proportional to the number density of X_u ions, n_u . On the other hand, stimulated emission does depend on the specific energy density of the incident radiation, u_ν . Thus, combining these two contributions, the rate at which emission from X_u to X_l happens, is:

$$\left(\frac{dn_l}{dt} \right)_{u \rightarrow l} = - \left(\frac{dn_u}{dt} \right)_{u \rightarrow l} = n_u (A_{ul} + B_{ul} u_\nu), \quad (56)$$

where the constants of proportionality, A_{ul} and B_{ul} , are the Einstein’s A and B coefficient for this particular transition (from X_u to X_l). Assuming thermal equilibrium between the radiation and the ions, the ratio n_u/n_l is given by the Boltzmann equation $n_u/n_l = (g_u/g_l)e^{-(E_u-E_l)/kT}$, where g_u and g_l are the statistical weights for the upper and lower level, respectively. Then, it can be shown that the three Einstein’s coefficients are related to each other as (Draine, 2011)

$$B_{ul} = \frac{c^3}{8\pi h \nu_{ul}^3} A_{ul} \quad (57)$$

$$B_{lu} = \frac{g_u}{g_l} B_{ul}, \quad (58)$$

Stimulated emission can be ignored in the IGM conditions, and thus we only need to consider spontaneous emission. In this case, the rates can be expressed as:

$$\left(\frac{dn_u}{dt} \right)_{l \rightarrow u} = n_l \frac{g_u}{g_l} \frac{c^3}{8\pi h \nu_{ul}^3} A_{ul}, \quad (59)$$

$$\left(\frac{dn_l}{dt} \right)_{u \rightarrow l} = n_u A_{ul}. \quad (60)$$

For specific ions and transitions, the Einstein's A and B coefficients can be determined from quantum mechanics and/or directly from experiments, and are usually tabulated (see Draine 2011 and references therein).

3.1.2 Modeling absorption lines

Absorption cross-section and the line profile

Interpreting absorption lines (e.g. those in the spectra of a background source that provides a continuum) requires modeling them in terms of the observed line profile and the absorption cross-section. In this case, the absorption cross-section, $\sigma_{lu}(\nu)$, can be defined by re-writing Equation 53 as (similar to the rates defined in Section 2.5.1),

$$\left(\frac{dn_u}{dt}\right)_{l \rightarrow u} = n_l \int \frac{u_\nu}{h\nu} \sigma_{lu}(\nu) c \, d\nu \approx n_l \frac{u_\nu}{h\nu_{ul}} c \int \sigma_{lu}(\nu) \, d\nu, \quad (61)$$

where the latter approximation assumes that u_ν and $h\nu$ are approximately constants over the absorption line profile given by $\sigma_{lu}(\nu)$. Comparing Equation 61 to Equations 53 and 59, we can relate the absorption cross-section to the Einstein's coefficients, as

$$\int \sigma_{lu}(\nu) \, d\nu = \frac{h\nu_{ul}}{c} B_{lu} = \frac{g_u}{g_l} \frac{c^2}{8\pi\nu_{ul}^2} A_{ul}. \quad (62)$$

From this, we can have an expression for the absorption cross-section in terms of the “natural line profile”, $\phi_{\text{nat.}}(\nu)$, as

$$\sigma_{lu}(\nu) = \frac{g_u}{g_l} \frac{c^2}{8\pi\nu_{ul}^2} A_{ul} \phi_{\text{nat.}}(\nu), \quad (63)$$

where $\phi_{\text{nat.}}(\nu)$ is a normalized function that encodes only the shape of the spectral line, i.e. it satisfies $\int \phi_{\text{nat.}}(\nu) \, d\nu = 1$.

At this point it is important to note that despite what its name may imply, an “absorption line” can be either produced by actual absorption of the photons into individual ions (excitation or ionization) and/or scattering (effectively an absorption and instantaneous re-emission), i.e. the ions just change the original trajectory of photons and scatter them away from the line-of-sight. In both cases the net effect is a deficit of photons from the background spectrum at specific frequencies producing an absorption line.

Oscillator strength

Another useful manner to quantify the strength of an absorption line produced by an ion in X_l being excited to X_u (Equation 52) is via the “oscillator strength”, f_{lu} . The oscillator strength is dimensionless and it corresponds to the probability of a transition between two quantum states due to interaction with electromagnetic radiation. In terms of the absorption cross-section it can be defined as,

$$f_{lu} = \frac{m_e c}{\pi e^2} \int \sigma_{lu}(\nu) \, d\nu, \quad (64)$$

and thus it is related to the natural absorption line profiles as:

$$\sigma_{lu}(\nu) = \frac{\pi e^2}{m_e c} f_{lu} \phi_{\text{nat.}}(\nu). \quad (65)$$

Of course, one can also find expressions of f_{lu} in terms of Einstein's coefficients (not done here, but see Draine 2011). For emission lines, the oscillator strength is defined to be negative, and the corresponding value for the particular emission line satisfies $f_{ul} = -\frac{g_l}{g_u} f_{lu}$. Similarly to the Einstein coefficients, the values of the oscillator strengths for different ion transitions can be computed from quantum mechanics and/or measured from experiments (Verner et al., 1994; Morton, 2003; Draine, 2011).

Line broadening

In practice, the *observed* line profile may differ from that of the natural profile, because of different physical processes. In the following we summarize the most important types of line broadening concerning IGM observations:¹³

- **Natural broadening:** The shape of $\phi_{\text{nat.}}(\nu)$ is driven by quantum mechanics. Although the line will be centred at frequency ν_{ul} , because of the uncertainty principle, $\Delta E \Delta t \geq \frac{\hbar}{4\pi}$, transitions from energy levels with larger lifetimes will have narrower line profiles, and vice-versa. The intrinsic natural line profile is well characterized by a Lorentzian function with a full-width at half maximum (FWHM) determined by the Einstein's A coefficients:

$$\text{FWHM}_{\phi_{\text{nat.}}} = \frac{1}{2\pi} \left(\sum_{E_i < E_u} A_{ui} + \sum_{E_i < E_l} A_{li} \right). \quad (66)$$

Note that for transitions where $l = 0$ (ground state) the second terms is zero. The Lorentzian profile is characterized by the damping parameter, γ_{lu} ($= \gamma_{ul}$), which is related to the FWHM as $\text{FWHM}_{\phi_{\text{nat.}}} = 2\pi/\gamma_{lu}$.

¹³But note that in other astrophysical contexts, other types of line broadening can be important too (e.g. collisional broadening).

- **Thermal broadening:** Thermal broadening (also known as Doppler broadening) occurs due to the random thermal motion of ions within the absorber. Each ion's rest-frame frequency of absorption (or emission) shifts to a different observed frequency because of the Doppler effect, which leads to a broadening of the spectral line. Assuming a Maxwellian velocity distribution for the ions, the resulting thermal line profile is Gaussian, with a corresponding 1-dimensional velocity standard deviation, $\sigma_v = \sqrt{\frac{kT}{m}}$, where m is the mass of the ion. The FWHM of the line profile is $\text{FWHM}_{\phi_{\text{th}}} = 2\sqrt{\ln 2}b_{\text{th}}$, with b_{th} being the so-called “Doppler parameter” defined as $b_{\text{th}} \equiv \sqrt{2}\sigma_v$.
- **Turbulent broadening:** Turbulent broadening is due to macroscopic motions within the absorber. While the exact nature and modeling of turbulence in astrophysical environments remain areas of active research, turbulent broadening is usually characterized by a “turbulent Doppler parameter”, b_{turb} , which is treated similarly to that of the thermal broadening such that the total Doppler parameter can be expressed as $b = \sqrt{b_{\text{th}}^2 + b_{\text{turb}}^2}$. However, in contrast to the thermal broadening, turbulent broadening is independent of the atomic mass of the ions, since it reflects the bulk motion of the gas as a whole rather than the random thermal motions of the individual particles.
- **Instrumental broadening:** Instrumental broadening (also known as the ‘line spread Function’, LSF) results from the finite resolution of spectrographs due to the combined telescope and instrument optics plus image quality (including the effects of the atmosphere, if any, e.g. the ‘seeing’). The instrumental profile sets the narrowest possible spectral line that can be observed, meaning that lines with physical FWHM smaller than this limit are *unresolved*. Typically, the instrumental broadening profile is characterized and known for a given spectrograph and thus can be properly accounted for when modeling absorption or emission lines. The shape of the LSF can vary from simple Gaussian profiles (most common case), to more complex shapes with no analytical description and thus are given as tabulated values instead.¹⁴

The Voigt profile

Given that the natural, thermal, and turbulent broadening processes are all present when observing absorption lines, the *actual* line profile ends up being a combination of Gaussian and Lorentzian profiles. This combination results in what is known as the Voigt profile, which represents the convolution of these two profiles (van de Hulst and Reesinck, 1947). Here, we will refer to this absorption line profile simply as ϕ_v^{Voigt} , which also satisfies $\int \phi_v^{\text{Voigt}} dv = 1$. In general, the Voigt profile should be used when measuring absorption lines for determining the properties of the absorbers. For this, dedicated open-source software is available for general use (e.g. Carswell and Webb, 2014; Hummels et al., 2017). Finally, the information from an individual Voigt profile fit is usually stored as a $(z_{\text{HI}}, N_{\text{HI}}, b_{\text{HI}})$ tuple.

Examples of Voigt profiles for H I Ly α with different column densities are given in Figure 7 (top panel). Weak (optically thin) absorption lines are dominated by the Gaussian component (in the core), while extremely saturated lines are dominated by the Lorentzian component instead (in the damping wings). In these extreme cases, the properties of the absorbers can often be directly inferred even from individual absorption lines (see ‘Curve of Growth’, below). For intermediate cases, there is a degeneracy between the intrinsic parameters, and thus more than one transition is usually required to determine column densities accurately. For more details about this Voigt profile, we refer the reader to Draine (2011).

Optical depth, column density, and equivalent width

In order to link the previous modeling of absorption lines with actual observations, we need to consider the radiative transfer equation. When the light of a quasar (or any other background source) passes through an intervening absorber, then its continuum intensity, I_ν , will be attenuated in proportion to both the absorption cross-section (σ_{lu}) and the density of ions that can produce the absorption (n_l). In the IGM conditions, the radiative transfer equation is simply (ignoring the emissivity term),

$$dI_\nu = -I_\nu \kappa_\nu ds, \quad (67)$$

where $\kappa_\nu \equiv n_l \sigma_{lu}(\nu)$ is the attenuation coefficient at frequency ν , and ds is the infinitesimal pathlength of propagation. For integrating this equation, it is convenient to define the “optical depth”, τ_ν , as satisfying,

$$d\tau_\nu \equiv \kappa_\nu ds, \quad (68)$$

such that Equation 67 becomes,

$$dI_\nu = -I_\nu d\tau_\nu. \quad (69)$$

The solution is then,

$$I_\nu(\tau_\nu) = I_\nu(0) \exp(-\tau_\nu), \quad (70)$$

where the $I_\nu(0)$ represents the intensity of radiation in the absence of the absorber. Assuming that the absorber completely covers the beam of the quasar, then we have a similar equation for the flux density, F_ν ,

$$F_\nu(\tau_\nu) = F_\nu(0) \exp(-\tau_\nu), \quad (71)$$

¹⁴e.g. The Cosmic Origin Spectrograph LSF is described in <https://www.stsci.edu/hst/instrumentation/cos/performance/spectral-resolution>

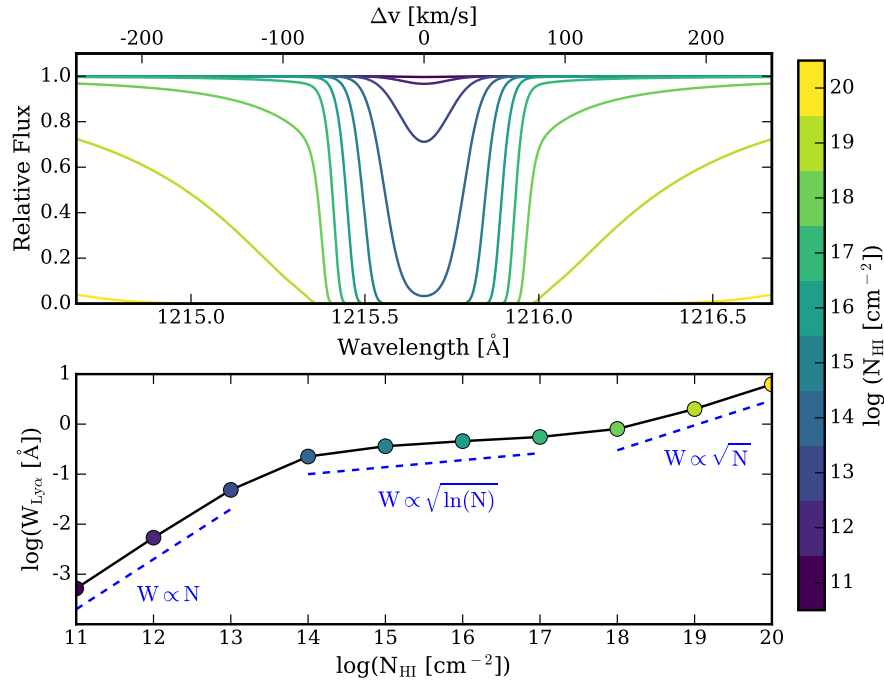


Fig. 7 Examples of theoretical absorption line profiles for the H I Ly α transition in a normalized spectrum (top) as a function of column density (see color bar) fixing the Doppler parameter to $b = 22 \text{ km s}^{-1}$, and the corresponding Curve of Growth (bottom). Figure from Hummels et al. (2017).

where $F_\nu(0)$ is the flux density of the source in the absence of the absorber, i.e. $F_\nu(\tau_\nu = 0)$. Thus, the quasar continuum spectrum will be exponentially attenuated at very specific frequencies (or wavelengths) given by the optical depth,

$$\tau_\nu = \int \kappa_\nu ds \quad (72)$$

$$= \int n_l \sigma_{lu}(\nu) ds \quad (73)$$

$$= \frac{\pi e^2}{m_e c} f_{lu} \int n_l \phi_\nu^{\text{Voigt}} ds, \quad (74)$$

where we have used Equations 68 and 65, respectively.

Given that the absorber can have a particular density profile, the density n_l should be a function of the pathlength, i.e. $n_l(s)$. However, the Voigt profile only depends on quantum mechanical properties of the ions, and the macroscopic properties of the absorber, like temperature and turbulence. It is usually assumed that within a single resolved absorption line, the temperature and turbulence are roughly constant, such that, ϕ_ν^{Voigt} is roughly independent of the pathlength, and thus

$$\tau_\nu \approx \frac{\pi e^2}{m_e c} f_{lu} \phi_\nu^{\text{Voigt}} \int n_l ds \quad (75)$$

$$= \frac{\pi e^2}{m_e c} f_{lu} \phi_\nu^{\text{Voigt}} N_l, \quad (76)$$

where,

$$N_l \equiv \int n_l ds, \quad (77)$$

is the column density. Therefore, the optical depth is directly proportional to the column density, the oscillator strength, and the Voigt profile,

$$\tau_\nu \propto N_l f_{lu} \phi_\nu^{\text{Voigt}}. \quad (78)$$

Similarly, if the density does not vary significantly along the pathlength, we can further infer that,

$$\tau_\nu \propto n_l f_{lu} \phi_\nu^{\text{Voigt}} \text{ (for } n_l = \text{const.)}. \quad (79)$$

Assuming the absorption lines are fully resolved by the spectrograph (i.e. the LSF is much narrower than the other line broadening mechanisms), then the Voigt profile is mostly determined by the quantum mechanical properties of the ion transition and the thermal (and/or turbulent) state of the absorber. In this case, we can use the shape and intensity of the absorption line to infer important physical parameters like their column densities and temperatures (and/or turbulence). However, in practice, because we do not always fully resolve the absorption profiles and/or the signal-to-noise (S/N) of the spectra is too low for properly characterizing the shape of the absorption line, these physical quantities are not readily accessible from this treatment. For these cases (and other uses) it is convenient to define the “equivalent width”, W , as

$$W \equiv \int \frac{F_\lambda(0) - F_\lambda(\tau_\lambda)}{F_\lambda(0)} d\lambda \quad (80)$$

$$= \int (1 - \exp(-\tau_\lambda)) d\lambda, \quad (81)$$

where τ_λ is the optical depth expressed as a function of wavelength, as we typically work with spectra given as a function of wavelength, F_λ . The equivalent width corresponds to the amount of flux “absorbed” relative to the continuum and has units of length.¹⁵ It is easy to show that W is independent of the resolving power of the spectrograph, which makes it a versatile observable which can (in some cases) be linked back to the more physical quantities of interest (e.g. column density) based on the “Curve of Growth”.

Curve of Growth

The relation between equivalent width (W) and column density (N_I) for a given ion transition is known as the Curve of Growth (COG). Given the definition of W , and the fact that $\tau_\lambda \propto N_I \phi_\lambda^{\text{Voigt}}$, then passing from known values of N_I and b to W is unambiguous. However, in practice one usually measures W and wishes to infer N_I , and the relation will depend on the value of b . Figure 7 (bottom panel) shows an example of a COG for the H I Ly α transition for a fixed Doppler parameter b . The optical depth at line-center, τ_0 , can be approximated by (Draine, 2011)

$$\tau_0 \approx \sqrt{\pi} \frac{e^2}{m_e c} \frac{N_I f_{lu} \lambda_{lu}}{b}, \quad (82)$$

where λ_{lu} is the wavelength associated to the transition. Here, it is important to emphasize that $\tau_0 \propto N_I/b$, thus for a given ion with a given τ_0 , broader absorption lines trace higher column densities.

Based on the value of τ_0 , the COG can be divided into three main regimes, each having a different dependence between W and N_I as follows:

- **Linear regime:** For $\tau_0 \lesssim 1$ (optically thin), the COG has a linear $W \propto N_I$ dependence, which is actually independent of b .
- **Flat regime:** When $10 \lesssim \tau_0 \lesssim 10^3$ (optically thick), the COG has a $W \propto b \sqrt{\ln(N_I/b)}$, hence a very mild (almost flat) dependence of W as a function of N_I . In this regime, the COG depends on b , and thus W is degenerate for some combinations of N_I and b .
- **Square root regime:** When $10^4 \lesssim \tau_0$ (optically thick), the COG has a $W \propto \sqrt{N_I}$ dependence, which is (again) independent of b .

Therefore, for the linear and square root regimes, it is relatively straightforward to infer N_I from W , even for isolated unresolved lines. However, this is generally not possible to do in the flat regime; even if one knows the value of b precisely, a small error in W propagates into a large error in N_I . For this latter case, one should attempt to use another transition(s) of the same ion falling into either the linear or the square root regime.¹⁶

Although the exact shape of the COG requires a proper integration of the Voigt profile (non-trivial), Draine (2011) provides a useful analytical approximation as

$$W \approx \begin{cases} \lambda_{lu} \sqrt{\pi} \frac{b}{c} \frac{\tau_0}{1 + \tau_0/(2\sqrt{2})} & \text{if } \tau_0 \leq 1.25393, \\ \lambda_{lu} \left[\left(\frac{2b}{c} \right)^2 \ln \left(\frac{\tau_0}{\ln 2} \right) + \frac{b}{c} \frac{\gamma_{lu} \lambda_{lu}}{c} \frac{(\tau_0 - 1.25393)}{\sqrt{\pi}} \right]^{1/2} & \text{if } \tau_0 > 1.25393. \end{cases} \quad (83)$$

For instance, evaluating Equation 82 for the H I Ly α transition at typical column density of $N_{\text{HI}} = 10^{13.5} \text{ cm}^{-2}$ and typical Doppler parameter of $b = 20 \text{ km s}^{-1}$, we obtain,

$$\tau_0 = 1.255 \left(\frac{N_I}{10^{13.5} \text{ cm}^{-2}} \right) \left(\frac{f_{lu}}{0.4164} \right) \left(\frac{\lambda_{lu}}{1215.67 \text{ \AA}} \right) \left(\frac{b}{20 \text{ km s}^{-1}} \right)^{-1}, \quad (84)$$

coinciding with the approximate limit between the linear and the flat portions of the COG (Equation 83). In contrast, the limit between the flat and square root portion of the COG will be at a $\approx 10^4$ larger column density, i.e. at $N_{\text{HI}} = 10^{17.5} \text{ cm}^{-2}$ (for the same $b = 20 \text{ km s}^{-1}$). These (and other) useful approximations and relations for the modeling and treatment of absorption lines are included in the open-source Python package LINETOOLS (Prochaska et al., 2017) for general use.

¹⁵For emission lines, the equivalent width is (by convention) negative, and it represents the amount of flux emitted relative to the continuum.

¹⁶For instance, for H I, if Ly α is in the flat regime, one could use Ly β or higher order Lyman series instead.

3.2 Observations of the IGM through quasar absorption lines

Quasar absorption lines have been extensively used to probe and study the IGM. Quasars allow us to probe the Universe since the EoR until the present day (Fan et al., 2023). In this Section, we will present a non-exhaustive review of strategies and observational methods for probing the IGM with quasar absorption lines.

3.2.1 The Gunn-Peterson effect

As mentioned in Section 1.2, an important early discovery was that of Gunn and Peterson (1965): the fact that we observe transmitted flux blueward of the Ly α emission of high- z quasars imply an extremely highly ionized IGM. The argument is simple but very powerful, summarized as follows.

The optical depth (τ_ν) of a single H I Ly α can be written as (Equation 73),

$$\tau_\nu = \int_0^s n_I(s) \sigma_{Ly\alpha}(\nu) ds \quad (85)$$

$$= \sigma_{Ly\alpha} \nu_{ul} \int_0^s n_I(s) \phi^{\text{Voigt}}(\nu) ds, \quad (86)$$

where $\sigma_{Ly\alpha} \equiv \frac{\pi e^2}{m_e c} \frac{f_{lu}}{\nu_{ul}} = 4.48 \times 10^{-18} \text{ cm}^2$ is the H I Ly α cross-section. If we consider the absorber to be at a cosmological redshift z , then $\frac{ds}{dz} = \frac{c}{H(z)(1+z)}$, and thus,

$$\tau_\nu = c \sigma_{Ly\alpha} \nu_{ul} \int_0^z n_I(z) \phi^{\text{Voigt}}(\nu) \frac{dz}{H(z)(1+z)}, \quad (87)$$

with $H(z) = H_0 \sqrt{\Omega_m(1+z)^3 + \Omega_\Lambda}$ for a flat Λ CDM cosmological model. Given that the line profile, $\phi^{\text{Voigt}}(\nu)$, strongly peaks at $\nu = \nu_{ul}/(1+z)$, then,

$$\tau_{Ly\alpha} = \sigma_{Ly\alpha} \frac{c}{H_0} \frac{n_{\text{HI}}(z)}{\sqrt{\Omega_m(1+z)^3 + \Omega_\Lambda}} \quad (88)$$

$$= \sigma_{Ly\alpha} \frac{c}{H_0} \frac{\langle n_{\text{H}} \rangle_0 (1+z)^3}{\sqrt{\Omega_m(1+z)^3 + \Omega_\Lambda}} x_{\text{HI}}(z), \quad (89)$$

where we have renamed n_I as n_{HI} , and τ_ν as $\tau_{Ly\alpha}$, and $x_{\text{HI}}(z)$ is the corresponding neutral fraction. Evaluating this equation for $H_0 = 70 \text{ km s}^{-1} \text{ Mpc}^{-1}$ and $\langle n_{\text{H}} \rangle_0 = 2.5 \times 10^{-7} \text{ cm}^{-3}$ (Equation 3), we obtain,

$$\tau_{Ly\alpha}(z) = 1.48 \times 10^4 x_{\text{HI}}(z) \frac{(1+z)^3}{\sqrt{\Omega_m(1+z)^3 + \Omega_\Lambda}}, \quad (90)$$

or,

$$x_{\text{HI}}(z) = 6.8 \times 10^{-5} \tau_{Ly\alpha}(z) \frac{\sqrt{\Omega_m(1+z)^3 + \Omega_\Lambda}}{(1+z)^3}. \quad (91)$$

Observations of the Ly α forest at $z \gtrsim 3$ indicate $\tau_{Ly\alpha} \lesssim 1$, while at $z \lesssim 1$ the $\tau_{Ly\alpha}$ are even smaller (see Figure 1). This implies that the x_{HI} must be extremely low (Gunn and Peterson, 1965): as reference, a $\tau_{Ly\alpha} \sim 1$ at $z = \{0, 3, 6\}$, corresponds to $x_{\text{HI}} \sim \{7, 0.5, 0.2\} \times 10^{-5}$, respectively. This is what is known as the ‘Gunn-Peterson effect’: only 1 neutral hydrogen per 10^5 or 10^6 ionized ones are sufficient to produce significant opacity. At $z \gtrsim 6$, the Universe becomes more neutral, and we can start to see spectral regions that are completely absorbed. These regions are known as ‘Gunn-Peterson troughs’ (e.g. see the highest redshift quasar in Figure 1; see also Fan et al. 2023), yet these could still be produced by a highly ionized medium, with $x_{\text{HI}} \sim 10^{-4}$. Flux transmission spikes between Gunn-Peterson troughs can be used to establish the sizes of early ionizing bubbles and constrain models for the ionizing sources (Fan et al., 2023).

3.2.2 Observational classification of H I absorbers

With sufficient spectral resolution, individual H I absorption lines can be resolved and we can study the different population of absorbers in more detail. Historically, H I absorbers are classified into different categories depending on their observational signatures imprinted in the quasar spectrum (e.g. Figure 8). More quantitatively, this classification depends on their column density as follows:

- **Ly α forest systems:** correspond to the weakest H I Ly α absorption lines at column densities of $N_{\text{HI}} \lesssim 10^{17.2} \text{ cm}^{-2}$. These are the most common absorption lines, and trace environments around the mean density of the Universe and up to mild overdensities $(1 + \delta) \lesssim 10$ (see Equation 51), i.e. the diffuse IGM. Their name comes from the fact that when observing a quasar spectrum, these absorption lines appear blueward of the quasar’s Ly α emission resembling a crowded “forest” (see Figures 1 and 8). A review article of these systems was written by Rauch (1998).
- **Lyman Limit systems (LLSs):** correspond to H I Ly α absorption lines at column densities $10^{17.2} \lesssim N_{\text{HI}} \lesssim 10^{20.3} \text{ cm}^{-2}$. At these higher column densities, it is possible to appreciate the Lyman limit break, a discontinuity at 912 \AA (in the rest-frame; equivalent to 13.6 eV) in the quasar spectrum, due to the lack of photons that are capable of fully ionizing the H I atoms in the absorber (see Figure 8).

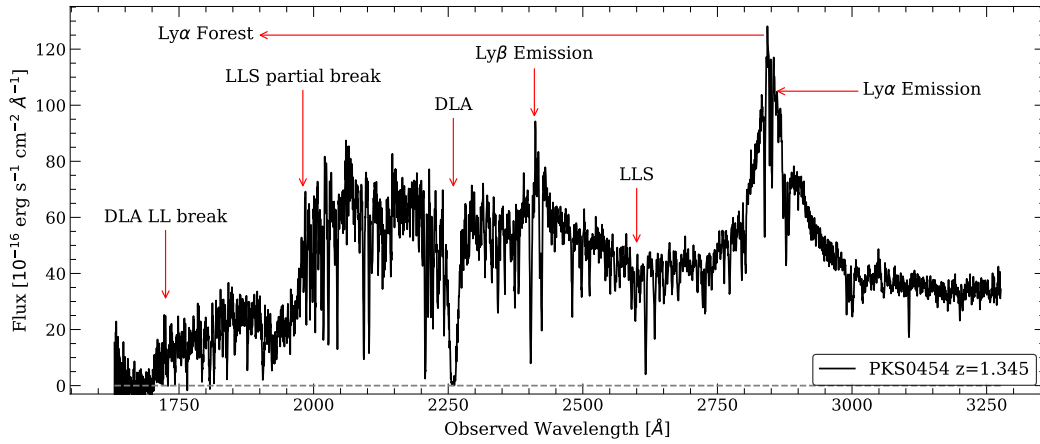


Fig. 8 Example of a quasar spectrum (PKS0454 at $z = 1.345$), where the different types of (intervening) H I absorbers are indicated (see Section 3.2.2). The H I Ly α and Ly β emission of the quasar itself are also marked. Figure credit: K. Martínez-Acosta (adapted from fig. 1 of Charlton and Churchill 2000).

Depending on whether the break reaches the zero level flux or not, these are referred to as LLSs or partial LLSs (pLLSs), respectively. The column density of $10^{17.2} \text{ cm}^{-2}$ corresponds to that of the inverse of the H I photoionization cross-section of $\sigma_{\text{p.i.}} = 6.3 \times 10^{-18} \text{ cm}^2$ (Equation 11). In terms of over-densities, these typically trace gas within or nearby galaxy halos, at $1 + \delta \gtrsim 100$. Some relevant articles about LLSs include Bahcall and Salpeter (1965); Tytler (1982); Songaila and Cowie (2010); Prochaska et al. (2010); Fumagalli et al. (2011); McQuinn et al. (2011); Lehner et al. (2013).

- **Damped Lyman- α systems (DLAs):** correspond to H I Ly α absorption lines at column densities $N_{\text{HI}} \gtrsim 10^{20.3} \text{ cm}^{-2}$. At these high column densities, it is possible to clearly appreciate the damping wings of the Lorentzian profile of the H I Ly α absorption line, even in low-resolution data (see Figure 8). This column density limit also corresponds to the transition towards a mostly neutral medium. In terms of over-densities, these are typically associated with environments near galaxy disks or within galaxies themselves (e.g. the ISM). A review article of these systems was written by Wolfe et al. (2005, see also Péroux and Howk 2020).

Despite this classification scheme being somewhat arbitrary (based on properties seen in the spectra of quasars), it is nevertheless sufficiently convenient that it is still being widely used. These categories resemble those of the COG (although not exactly). Ly α forest absorbers are associated with the linear and flat portions of the COG, while LLS and DLAs are associated to the square root portion of it. Among these three, the LLSs are the most difficult to model given the uncertainties in the ionization corrections (among other issues); in contrast, DLAs are mostly neutral absorbers, while Ly α forest systems are mostly ionized. For characterizing LLS, it is usually required to have several of the Lyman series lines modeled simultaneously (covering different regimes in the COG), and also include the Lyman Limit break intensity. Some authors even define an intermediate category between LLSs and DLAs, at $10^{19} \lesssim N_{\text{HI}} \lesssim 10^{20.3} \text{ cm}^{-2}$, referred to as super-LLS or sub-DLAs systems, which speaks of the complexity of the transition from LLS to DLA (Péroux and Howk, 2020).

3.2.3 Surveys of H I absorbers

In order to study these H I absorbers at different redshifts and/or environments, we require observational surveys. A survey is typically constructed by using a sample of spectra of background quasars to search and characterize absorption lines. The majority of these absorption lines at observed wavelengths shorter than the H I Ly α emission of the quasar, $\lambda_{\text{obs}} < \lambda_{\text{qso}}^{\text{Ly}\alpha} = 1215.67 \text{ Å} (1 + z_{\text{qso}})$ will correspond to H I (e.g. the Ly α -forest), but some can also be produced by helium, metals or even molecules. Indeed, at $\lambda_{\text{obs}} > \lambda_{\text{qso}}^{\text{Ly}\alpha}$ the majority will be from metal ions. These absorption lines will be produced by absorbers at redshifts $z_{\text{abs}} \leq z_{\text{qso}}$, and thus it is convenient to use them to probe different cosmic epochs.

The incidence of H I absorbers

A key observable is the incidence of absorption lines per unit redshift,

$$\frac{dN_{\text{abs}}}{dz} = \frac{N_{\text{abs}}(W_r \geq W_{r,\text{min}})}{\Delta z(W_r \geq W_{r,\text{min}})}, \quad (92)$$

where N_{abs} is the actual number of absorption lines with rest-frame equivalent width, W_r ,¹⁷ larger than a minimum threshold, $W_{r,\text{min}}$, found

¹⁷The rest-frame equivalent width is related to the observed equivalent width by $W_r = W_{\text{obs}}/(1 + z)$.

within a given “redshift path”, Δz , defined as the redshift range where absorption lines of $W_r > W_{r,\min}$ could have been observed if these were present. The redshift path corresponds to the (1-dimensional) searching “volume”, and it depends on S/N and/or wavelength coverage of the quasar spectra; in contrast to surveys that rely on emission (e.g. galaxy surveys), the selection function for detecting absorbers within a quasar sightline is fairly uniform with redshift. \mathcal{N}_{abs} and Δz can be constructed by summing up the contributions from the different quasar sightlines in a given survey, and they can be split into specific redshift ranges and/or intrinsic properties of the absorbers (e.g. column density).

If we model absorbers as discrete “clouds”¹⁸ that produce the individual absorption lines we see in the spectra of quasars, we can relate the $d\mathcal{N}_{\text{abs}}/dz$ to their volumetric number density, $n_{\text{abs}}(z)$, and (proper) cross-section, $\sigma_{\text{abs}}(z)$, as

$$\frac{d\mathcal{N}_{\text{abs}}}{dz} = \frac{c}{H_0} n_{\text{abs}}(z) \sigma_{\text{abs}}(z) \frac{dX}{dz}, \quad (93)$$

where dX/dz is the differential “absorption distance” defined below.¹⁹ If we observe a redshift evolution in $d\mathcal{N}_{\text{abs}}/dz$, it could be intrinsic to the absorbers themselves and/or simply due to the expansion of the Universe. In order to account for the latter, dX/dz relates the proper absorption distance to the redshift path due to the Universe’s expansion (Bahcall and Peebles, 1969),

$$\frac{dX}{dz} \equiv \frac{(1+z)^2}{\sqrt{\Omega_m(1+z)^3 + \Omega_\Lambda}}, \quad (94)$$

for a flat Λ CDM Universe at late times, such that

$$\frac{d\mathcal{N}_{\text{abs}}}{dz} = \mathcal{N}_{\text{abs}}(z) \frac{dX}{dz}, \quad (95)$$

where $\mathcal{N}_{\text{abs}}(z) = \frac{c}{H_0} n_{\text{abs}}(z) \sigma_{\text{abs}}(z)$. This term can be parametrized as a power-law of the form,

$$\mathcal{N}_{\text{abs}}(z) = \mathcal{N}_{\text{abs},0} (1+z)^\epsilon, \quad (96)$$

such that Equation 93 can be written as,

$$\frac{d\mathcal{N}_{\text{abs}}}{dz} = \mathcal{N}_{\text{abs},0} \frac{(1+z)^{2+\epsilon}}{\sqrt{\Omega_m(1+z)^3 + \Omega_\Lambda}}. \quad (97)$$

Modeling the observed $d\mathcal{N}_{\text{abs}}/dz$ in this manner, one can establish the value of ϵ . If $\epsilon \approx 0$ then the absorbers are not evolving significantly. Here we note that some studies parametrize $d\mathcal{N}_{\text{abs}}/dz$ as²⁰

$$\frac{d\mathcal{N}_{\text{abs}}}{dz} = \mathcal{N}_{\text{abs},0} (1+z)^{\gamma_n}, \quad (98)$$

instead (e.g. Janknecht et al. 2006; Kim et al. 2021) but the main idea remains the same: by measuring γ_n one can establish if absorbers are intrinsically evolving or not. These studies have revealed that at $z > 2$, $\mathcal{N}_{\text{abs}}(z)$ shows significant evolution, with $\gamma_n > 1 - 2$, whereas at $z \lesssim 1$, $d\mathcal{N}_{\text{abs}}/dz$ is consistent with following the expectation from cosmic expansion (Janknecht et al., 2006; Kim et al., 2021). An evolution in $\mathcal{N}_{\text{abs}}(z)$ can be interpreted as an evolution of either the number density or the cross-section of the absorbers, as this technique is only sensible to the product of $n_{\text{abs}}(z) \sigma_{\text{abs}}(z)$.

The H I column density distribution

As seen before, not all H I absorbers probe the same medium, as their properties will depend on density, temperature, ionization condition, etc. Empirically, we observe that low- N_{HI} absorbers are much more common than high- N_{HI} absorbers. Based on the previous analysis this could imply that low- N_{HI} absorbers are either more numerous and/or have larger cross-sections than their high- N_{HI} counterparts. Independently of the interpretation, the column density distribution of H I is a key observable that has been widely used to shed light into the nature of absorbers, and their importance in cosmology and astrophysics.

The H I column density distribution is defined as

$$f(N_{\text{HI}}, z) \equiv \frac{\partial^2 \mathcal{N}_{\text{abs}}}{\partial N_{\text{HI}} \partial X} = \frac{\partial^2 \mathcal{N}_{\text{abs}}}{\partial N_{\text{HI}} \partial z} \frac{\sqrt{\Omega_m(1+z)^3 + \Omega_\Lambda}}{(1+z)^2}, \quad (99)$$

again, the $(dX/dz)^{-1}$ term ensures that $f(N_{\text{HI}}, z)$ is constant if \mathcal{N}_{abs} does not evolve with z . $f(N_{\text{HI}}, z)$ can be inferred directly from quasar observations by establishing their $d\mathcal{N}_{\text{abs}}/dz$ as a function of N_{HI} . Typically, $f(N_{\text{HI}}, z)$ is parametrized as a power-law of the form,

$$f(N_{\text{HI}}, z) = C N_{\text{HI}}^{-\beta_n} (1+z)^{\gamma_n}, \quad (100)$$

with C a constant and $\beta_n > 0$, although the explicit dependency on z is sometimes not given when the measurements are performed over

¹⁸But note these do not need to have a spherical geometry. Indeed, at $1 + \delta \lesssim 10$ we expect these to be distributed in sheet-like or filamentary structures following the dark matter ‘cosmic web’, rather than halos.

¹⁹We note that Equation 93 assumes unity covering fraction, but this could be easily relaxed by adding a f_c term representing it.

²⁰For early studies, this parametrization made sense as the Λ CDM cosmology was not established and thus $\Omega_\Lambda = 0$.

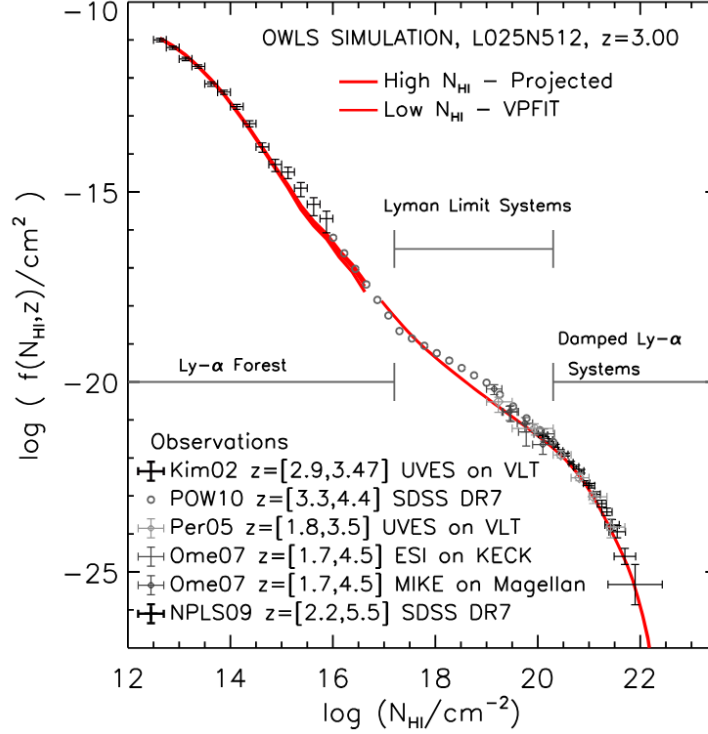


Fig. 9 Model and observational constraints for the H I column density distribution at $2 \lesssim z \lesssim 5$. The model of Altay et al. (2011) is shown by the red curve, based on a cosmological hydrodynamical simulation evaluated at $z = 3$. Figure from Altay et al. (2011).

narrow redshift ranges (Tytler, 1982; Janknecht et al., 2006; Danforth et al., 2016).

The shape of $f(N_{\text{HI}}, z)$ can be used to constrain Γ_{HI} (e.g. via Equation 50) and is also important for estimating the total mass budget in the IGM traced by H I absorbers (see below). Depending on the range of N_{HI} covered, and/or the statistical precision in the measurements, deviations from a single power-law have been reported; indeed, whether a single or a multiple power-law model (with different $-\beta_n$ slopes) is required to fit the $f(N_{\text{HI}}, z)$ can be interpreted as evidence for single or multiple populations of H I absorbers (Tytler, 1982; Prochaska et al., 2010; Kim et al., 2021).

To go beyond concatenations of different power-laws, it is convenient to rely on cosmological hydrodynamical simulations. Figure 9 shows a compilation of several observational works that estimate $f(N_{\text{HI}}, z)$ at $z \gtrsim 3$ for different ranges of N_{HI} , together with a modeling based on a cosmological hydrodynamical simulation at $z = 3$ presented by Altay et al. (2011). Their model includes ionization corrections and self-shielding (Zheng and Miralda-Escudé, 2002) that affect the absorbers at $N_{\text{HI}} \gtrsim 10^{17.2} \text{ cm}^{-2}$ (LLSs), as well as the transition to a mostly neutral medium at higher $N_{\text{HI}} \gtrsim 10^{20.3} \text{ cm}^{-2}$ (DLAs). At even higher $N_{\text{HI}} \gtrsim 10^{21.5} \text{ cm}^{-2}$, they also model the effects of molecular hydrogen gas (H_2) and star formation. These results shed light into the origin of the H I absorbers, where changes in the slope of the $f(N_{\text{HI}}, z)$ can be attributed to changes in the physical conditions of the absorbing gas. The remarkable agreement between observations and theory (over 10 orders of magnitude in N_{HI} !) indicates that our general understanding of the physical origin of H I absorbers is robust.

Baryon budget of the H I absorbers

At a given redshift, the average mass density traced by H I absorbers can be obtained by integrating the $f(N_{\text{HI}}, z)$ over all H I column densities and correcting for ionization. Parametrizing this gas density in units of the critical density of the Universe, ρ_c , we have (Schaye, 2001)

$$\Omega_g(z) = \frac{8\pi G m_{\text{H}}}{3H_0 c(1-Y)} \int \frac{n_{\text{H}}}{n_{\text{HI}}} N_{\text{HI}} f(N_{\text{HI}}, z) dN_{\text{HI}}. \quad (101)$$

where Y is the baryonic mass fraction in helium ($Y = 0.24$). Restricting this analysis to the diffuse IGM, and assuming the absorbers are in local hydrostatic equilibrium (Section 2.6), then combining Equations 27, 37 and 49 imply (Schaye, 2001)

$$\Omega_g(z) \approx 3.1 \times 10^{-9} \left(\frac{\Gamma_{\text{HI}}}{10^{-12} \text{ s}^{-1}} \right)^{1/3} \left(\frac{f_g}{0.17} \right)^{1/2} \left(\frac{T}{10^4 \text{ K}} \right)^{0.59} \int N_{\text{HI}}^{1/3} f(N_{\text{HI}}, z) dN_{\text{HI}}. \quad (102)$$

here we have assumed a value of $H_0 = 70 \text{ km s}^{-1} \text{ Mpc}^{-1}$, and that the temperature does not vary strongly as a function of N_{HI} . Evaluating

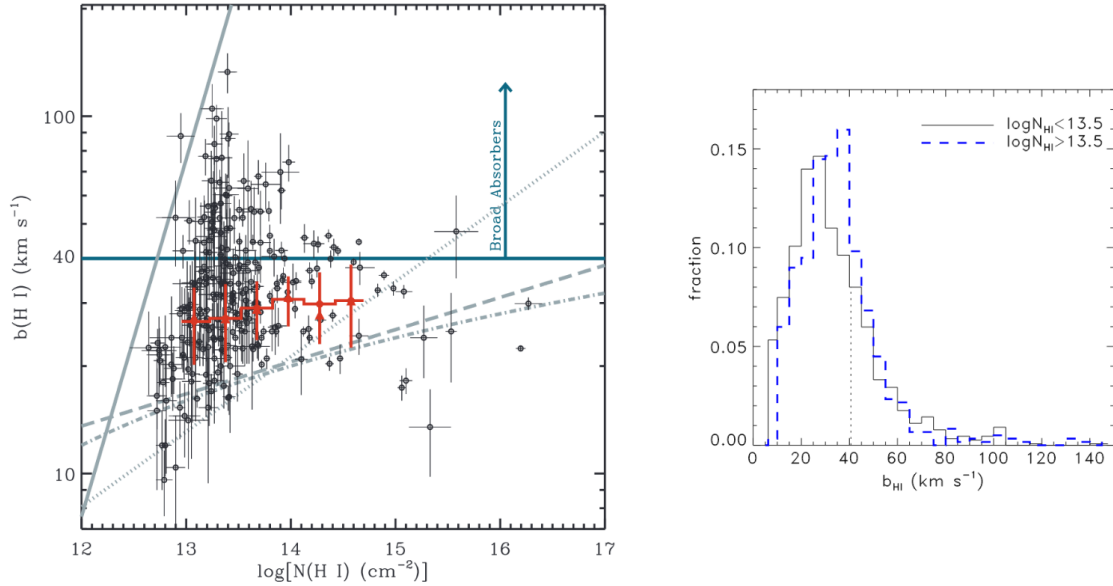


Fig. 10 Left: A Doppler parameter versus column density diagram for H I absorbers at $z \lesssim 0.4$ from Lehner et al. (2007). The solid line marks the observational limit of their survey, such that lines at the left of this line are missed. The dotted grey line shows the predicted minimum b_{HI} according to hydrodynamical simulations. The dashed and dotted-dashed lines show the observed lower envelope for a sample of high redshift H I absorbers (see references in Lehner et al. 2007). The horizontal solid line represent the typical limit between broad and narrow H I absorbers at $b_{\text{HI}} = 40 \text{ km s}^{-1}$ (corresponding to $T = 10^5 \text{ K}$ assuming no turbulence). Finally, the red points show the mean (circles) and median (triangles) b_{HI} values for six bins in N_{HI} restricting to just absorbers with $b < 40 \text{ km s}^{-1}$. Figure from Lehner et al. (2007). Right: H I Doppler parameter distribution for $N_{\text{HI}} < 10^{13.5} \text{ cm}^{-2}$ (solid black) and $N_{\text{HI}} > 10^{13.5} \text{ cm}^{-2}$ (dashed blue) absorbers at $z \lesssim 0.5$. Figure from Danforth et al. (2016).

$f(N_{\text{HI}}, z)$ and integrating over typical Ly α forest lines at $z \gtrsim 3$ provide $\Omega_g \sim \Omega_b$, implying that the vast majority of baryons are in the diffuse IGM at these high redshifts (Fukugita et al., 1998; Schaye, 2001). However, the same calculation at $z \lesssim 0.5$ only accounts for $\Omega_g \sim 0.3\Omega_b$ (Shull et al., 2012). Intriguingly, condensed matter in the CGM or within galaxies (cold gas, dust, stars, etc.) and hot gas in galaxy clusters (e.g. traced by X-ray emission) at $z \sim 0$ only account for $\sim 0.1\Omega_b$ (Bregman, 2007; Shull et al., 2012). This $\sim 50\%$ deficit of baryons in the low- z Universe is known as the ‘missing baryon problem’ (Fukugita et al., 1998). According to hydrodynamical simulations, these missing baryons are in the WHIM (Cen and Ostriker 1999; Davé et al. 2001; Cen and Ostriker 2006; Shull et al. 2012; see Figure 3), which have eluded a firm observational confirmation from our traditional techniques (quasar absorption lines and/or X-ray emission) due to their lack of sensitivity. However, complementary observational techniques are now allowing us to directly detect all these baryons (see Section 4.1).

The H I Doppler parameter distribution

Another important observable from H I absorbers is the distribution of Doppler parameters, b_{HI} . Doppler parameters encode thermal and/or non-thermal broadening (e.g. turbulence), characterized as (see Section 3.1.2)

$$b_{\text{HI}} = \sqrt{\frac{2kT}{m_{\text{H}}} + b_{\text{turb.}}^2}. \quad (103)$$

Therefore, we can use b_{HI} to constrain the temperature of the IGM, given some assumptions or estimations for $b_{\text{turb.}}$. For instance, one can treat the inferred T from b_{HI} as a lower limit (i.e. there is no knowledge of $b_{\text{turb.}}$) and fit for a density-temperature relation (see Section 2.5.2) in the lower envelope of a $b_{\text{HI}}-N_{\text{HI}}$ diagram (Schaye et al. 2000; Kim et al. 2001; Lehner et al. 2007; see Figure 10, left panel). Alternatively, one can use metal ion absorbers that are aligned (kinematically) with the H I and disentangle $b_{\text{turb.}}$, by assuming that the both the H I and the metal ion absorption are probing the same gas phase (e.g. Savage et al. 2014; although see Marra et al. 2024). Even for non-resolved absorption lines (especially relevant for the crowded Ly α forest at high- z), one can still use the shape of the line-profile at the line centers to constrain T (Lidz et al., 2010). Empirically, the b_{HI} distribution is well characterized by a log-normal function, with a peak at around $b_{\text{HI}}^{\text{peak}} \sim 20 - 30 \text{ km s}^{-1}$ and an extended tail towards larger values, $b_{\text{HI}}^{\text{tail}} \sim 100 \text{ km s}^{-1}$ (Lehner et al. 2007; Danforth et al. 2016; see Figure 10, right panel). These kind of measurements indicate that the temperature of the diffuse IGM at mean density is of order $T \approx 0.5 - 2 \times 10^4 \text{ K}$, depending on redshift (e.g. Schaye et al. 2000; see Figure 6).

Assuming no turbulent broadening, then $T > 10^5 \text{ K}$ would correspond to $b_{\text{HI}} > 40 \text{ km s}^{-1}$; therefore, the tail at $b_{\text{HI}} \gtrsim 40 \text{ km s}^{-1}$ could be partly due to the WHIM (Richter et al., 2006; Danforth et al., 2010). However, empirically establishing the temperature for these broad H I absorbers (BLAs) has turned out to be very difficult. Apart from the uncertainties associated with estimating $b_{\text{turb.}}$, these absorbers require

higher S/N and higher resolution given their intrinsically smaller τ_0 (for a fixed N_{HI} ; see Equation 82) and are more likely to blend with nearby systems (Richter et al., 2006). Still, there has been observational evidence of a possible excess of BLAs in inter-cluster filaments, which could be an indirect signature of the WHIM (Tejos et al. 2016).

The connection between H I Ly α absorbers and galaxies

According to the Λ CDM paradigm, galaxies and gas in the IGM are both distributed following the same cosmic web shaped by dark matter and dark energy. Yet, testing this prediction has been challenging, because this requires having sufficient data on galaxies and IGM absorbers in the same volumes and over Mpc scales. At $z \lesssim 0.5$, where we have a relatively good mapping of galaxies, we require (restrictive) space-based UV spectroscopy to access H I. In contrast, at $z \gtrsim 2$, we have a good mapping of H I via optical spectroscopy, but we lack sufficient mapping of galaxies. Early studies at $z \lesssim 0.5$ established a spatial correlation between H I and galaxies, leading to two main interpretations: i) H I absorbers are part of extended galaxy halos (e.g. Lanzetta et al., 1995), and ii) H I absorbers are correlated with galaxies mostly because they both trace the same underlying matter distribution but are not necessarily the same physical systems (e.g. Morris et al., 1993). Later studies confirmed that the relative importance of these two interpretations depends on N_{HI} : at $N_{\text{HI}} \gtrsim 10^{15} \text{ cm}^{-2}$, the absorbers are mostly related to the CGM (i.e. galaxy halos), whereas at $N_{\text{HI}} \lesssim 10^{15} \text{ cm}^{-2}$, the absorbers are mostly tracing the diffuse IGM in the large-scale structure (Chen et al., 2005; Prochaska et al., 2011; Tejos et al., 2014; Burchett et al., 2020). Similar conclusions can be reached from observations at $z \gtrsim 2$ (Adelberger et al., 2003, 2005; Rudie et al., 2012). Interestingly, observations have also established the existence of a population of H I absorbers that reside within galaxy voids (Penton et al., 2002; Tejos et al., 2012), which are not correlated with galaxies at all (Tejos et al., 2014).

Metals and enrichment of the IGM

Although in this Chapter we have focused on mostly on H I absorbers, some of the methodologies presented can also be applied to other ions, including metals. The metal enrichment of the IGM is an important observable for constraining galaxy evolution models, as metals must originate within galaxies (Theuns et al., 2002; Scannapieco et al., 2002; Oppenheimer and Davé, 2006). Current observations of resolved metal absorption lines are mostly tracing CGM or galaxy environments (Ellison et al., 2000; Tripp et al., 2008; D’Odorico et al., 2016; Péroux and Howk, 2020) but some intervening high-ionization ions like O VI, O VII and N V may be tracing some (high-density) regions of the WHIM (Tumlinson et al., 2017; Nicastro et al., 2018; Artale et al., 2022). Similar conclusions can be reached from studies from unresolved lines (Aracil et al., 2004). We refer the reader to Chapters “Circumgalactic medium”, “Galactic winds and outflows” and “First galaxies” for more discussion on metal ions.

Global pixel-by-pixel statistics

When individual absorption lines are not resolved, it is still possible to obtain relevant information from quasar spectroscopy. One such example is the Gunn-Peterson Effect described earlier. Similarly, under the assumption that the opacity in a given pixel is dominated by H I absorbers in the highly ionized diffuse IGM (Ly α -forest) in PIE (Equation 37) at a single density and temperature (Equation 79) following the temperature-density relation (Equation 46), we have

$$\tau_{\text{Ly}\alpha} \propto n_{\text{HI}} \propto n_{\text{H}}^2 \alpha_A(T) \Gamma_{\text{HI}}^{-1} \propto n_{\text{H}}^2 T^{-0.71} \Gamma_{\text{HI}}^{-1} \propto n_{\text{H}}^{1.58} \Gamma_{\text{HI}}^{-1} \quad (104)$$

$$\tau_{\text{Ly}\alpha} \propto (1 + \delta)^{1.58}, \quad (105)$$

meaning that fluctuations in τ_{r} can be used to estimate fluctuations in the underlying density field. This is known as the ‘fluctuating Gunn-Peterson approximation’ and is widely used to test models of structure formation and infer physical parameters of the IGM (see Chapter “Cosmology with the Lyman- α forest”). Other important measurements include the power-spectrum and the mean transmission flux distribution of the Ly α -forest, which can also be used to constrain the nature of dark matter and test our cosmological paradigm (Croft et al., 1998; Zaldarriaga et al., 2001; Viel et al., 2004; McDonald et al., 2005; Becker et al., 2013). We refer the reader to Chapters “Linear structure formation”, “Power spectra and correlation functions”, “Baryon acoustic oscillations” and “Cosmology with the Lyman- α forest” for more details on cosmological applications.

4 Concluding remarks and future prospects

The IGM remains indispensable for shaping our understanding of cosmology and galaxy evolution. As the reservoir of most of the baryonic matter in the Universe, it is fundamental to the processes that govern large-scale structure formation and the baryon cycle of galaxies. Although the physics of the IGM is relatively well understood, there are still key questions that are important to address in the nearby future. Some of these include:

- Where are the ‘missing baryons’?
- Is there really a WHIM, as hydrodynamical simulations predict?
- If the WHIM exists, what are its typical densities, temperatures, and environments?
- How important are galaxy feedback processes in injecting energy to the WHIM and the rest of the IGM?
- What is the metallicity of the IGM (beyond galaxy halos) as a function of cosmic environment and redshift?

- What are the sources of the UVB that ionized the IGM during and after EoR?
- What are the sources of the UVB that ionized He II at $z \sim 3$?
- What is the shape of the baryonic cosmic web in relation to that of dark matter (beyond 2-point statistics)? Are baryons distributed in a one-to-one correspondence with dark matter? Does this still hold on scales closer to that of galaxy halos?
- What is the relation of the underdense IGM and galaxies in the cosmic web (e.g. galaxy voids)?
- What are the strengths and relative importance of magnetic fields?

Quasar spectroscopy has been fundamental for establishing our current knowledge of the IGM, but this technique alone may not be enough to answer all these pressing questions. New discoveries and new technologies have enabled the development of complementary observational techniques that can help address these and future questions regarding the IGM.

4.1 Other complementary observational techniques

For advancing our understanding of the IGM, we must rely on complementary techniques to that of quasar spectroscopy. In the following, we briefly mention some of these:

- **Probing the IGM with fast radio bursts (FRBs):** FRBs are extragalactic millisecond radio pulses of yet unknown origin (Lorimer et al. 2007; Cordes and Chatterjee 2019; see Chapter “Fast radio bursts”). The dispersion measure of FRBs is $DM = \int n_e ds$, and thus these pulses can be used to directly trace ionized baryons in the IGM, independent of temperature. This technique requires isolating the intergalactic DM contribution out of the total observed DM. A recent application of this concept has confirmed that all the expected baryons are indeed in a highly ionized medium, thus conclusively solving the ‘missing baryon’ problem (Macquart et al. 2020; see also Chapter “Cosmology with fast radio bursts”). However, the exact location of these baryons in relation to the cosmic web and/or galaxy halos (e.g. IGM versus CGM) is still unknown; addressing this issue requires a sufficiently complete mapping of large-scale structures towards FRB sightlines (Khrykin et al., 2024). Moreover, FRBs can also constrain the magnetic fields via their rotation measures, and also have the potential to constrain He II reionization if observed at $z \gtrsim 3$ (see Chapter “Cosmology with fast radio bursts”).
- **Detecting the WHIM with the thermal Sunyaev-Zeldovich (tSZ) effect:** The tSZ effect is produced by Compton scattering of CMB photons that interact with electrons in a hot medium (Sunyaev and Zeldovich, 1972). This technique provides a signal that is $\propto \int n_e T ds$ of the intervening gas, and therefore could be used to detect and characterize the WHIM, assuming there is independent knowledge of n_e . Recent studies have detected a positive signal from the stacking of the tSZ maps over large samples of massive galaxy pairs that could be intergalactic (de Graaff et al., 2019). These authors combined their tSZ signal with weak lensing mass estimates to infer that their stacked signal comes from overdensities of $1 + \delta \approx 5$ and a temperature close to $T \approx 3 \times 10^6$ K, i.e. comparable to those of a WHIM. Future higher resolution tSZ maps (e.g. Ade et al. 2019), in combination with weak-lensing mass estimates, can thus provide further evidence for the WHIM.
- **Probing the IGM with X-ray emission:** In the low redshift Universe, one of the best prospects for detecting the IGM in emission is via X-ray imaging of the WHIM. Bremsstrahlung (free-free emission) in a hot medium produce X-ray photons, as commonly observed in the ICM of galaxy clusters (see Chapter “Galaxy clusters and the local Universe”). This emission is $\propto n_e n_{\text{H}} \sqrt{T}$, i.e. $\propto n_{\text{H}}^2 \sqrt{T}$ in a highly ionized medium. The temperature can be determined via the frequency cut-off of the emission, thus X-ray imaging and spectroscopy can be used to constrain both the density and temperature of the gas. With current sensitivities, some detections of IGM material in inter-cluster filaments have already been reported with inferred overdensities of $1 + \delta \approx 150$ and temperatures $T \sim 10^7$ K (Werner et al., 2008). These are at the limit between WHIM and ‘Hot Gas’ phases, and is still unclear whether the CGM of massive galaxies or groups are affecting the results. Current and next generation of X-ray missions (including the recent eROSITA survey; Merloni et al. 2024; Zhang et al. 2024) will allow us to push the limits towards densities and temperatures more comparable with those of the WHIM.
- **Probing the IGM with Ly α -emission:** At higher redshifts, probably the best strategy for observing the IGM in emission is through Ly α emission itself. Although this is beyond current capabilities for typical column densities of the Ly α -forest absorbers, it is expected that the fluorescent Ly α emission produced by the outer layers of optically thick self-shielded clouds (e.g. LLS) may be within reach. Indeed, Cantalupo et al. (2014) reported such an emission at intergalactic distances aided by the extra radiation field of a nearby quasar at $z \sim 2.3$. Whether the signal is truly intergalactic or not is still unclear. For instance, Gallego et al. (2018) stacked on pairs of Ly α -emitters (galaxies) at $3 < z < 4$ to search for this signal and could only detect a signal from the CGM of these galaxies rather than being intergalactic (Wisotzki et al., 2018). Still, future 30-m will have the sensitivities to attempt this experiment more efficiently.
- **Probing the IGM with multiple sightlines:** It is possible to extend the traditional quasar absorption line spectroscopy technique (limited to probing gas only in the line-of-sight direction) to study correlations in the transverse direction by using multiple quasars pairs, either binaries or strongly lensed systems. This has been already fundamental to measure the coherence lengths and establish the three-dimensional distribution and geometries of H I (and metal) absorbers (Dinshaw et al., 1994; Smette et al., 1995; Fang et al., 1996; Rauch et al., 2005; Rorai et al., 2013). Similarly, gravitational-arcs as background sources can provide multiple and contiguous coverage over several 100 kpc^2 for intervening material (Lopez et al., 2018). Moreover, the use of background galaxies as background sources allow us to probe the IGM with a much finer sampling than what quasars pairs can afford; this concept has been recently applied to provide the first Ly α -forest tomography of the cosmic web at $z > 2$ (Lee et al., 2018). The next generation of 30-m optical telescopes will be able to routinely achieve this kind of mapping (Japelj et al., 2019).
- **Probing the IGM with gamma-ray bursts (GRBs):** GRBs are bright short-lived bursts of gamma-ray radiation from highly energetic cosmic explosions, often associated with the collapse of massive stars or the merger of compact objects like neutron stars (see Chap-

ter “Gamma-ray bursts”). GRBs optical afterglows can be used to probe the IGM in a similar fashion as quasars, i.e. via spectroscopic analysis of their intervening absorption lines. The novelty here is that these afterglows are transient, and thus they eventually fade away. This allows for more sensitive search of intervening galaxies that could be associated to H I absorbers compared to those around quasars (Chen et al., 2005). Moreover, the energetics of GRBs imply that we could detect them at $z \gtrsim 8$ (Salvaterra et al., 2009), thus these could also help us to constrain the physics of the EoR.

Achieving a comprehensive understanding of the IGM requires further observational data and refined theoretical models to capture its complex behavior across cosmic time and environments. By continuously studying and analyzing the light from various distant objects, we can refine our understanding of the IGM and its role in the cosmic landscape.

Acknowledgments

We thank Joe N. Burchett, Sebastián López, J. Xavier Prochaska, and Jessica Werk for their comments and suggestions on the manuscript. We are also grateful to Karen Martínez–Acosta for providing the figures with the quasar spectra. Additionally, we thank Gabriel Altay, Renyue Cen, Charles Danforth, Daniela Galárraga–Espinosa, Cameron Hummels, Vikram Khaire, Nicolas Lehner, Davide Martizzi, Rüdiger Pakmor, and Phoebe Upton–Sanderbeck for granting permission to use their figures as part of this Chapter.

See Also: Rauch (1998); Meiksin (2009); Draine (2011); McQuinn (2016); Tumlinson et al. (2017); Péroux and Howk (2020); Faucher-Giguère and Oh (2023).

References

- Ade P, Aguirre J, Ahmed Z, Aiola S, Ali A, Alonso D, Alvarez MA, Arnold K, Ashton P, Austermann J, Awan H, Baccigalupi C, Baidon T, Barron D, Battaglia N, Batty R, Baxter E, Bazarko A, Beall JA, Bean R, Beck D, Beckman S, Beringue B, Bianchini F, Boada S, Boettger D, Bond JR, Borrill J, Brown ML, Bruno SM, Bryan S, Calabrese E, Calafut V, Calisse P, Carron J, Challinor A, Chesmore G, Chinone Y, Chluba J, Cho HMS, Choi S, Coppi G, Cothard NF, Coughlin K, Crichton D, Crowley KD, Crowley KT, Cukierman A, D'Ewart JM, Dünner R, de Haan T, Devlin M, Dicker S, Didier J, Dobbs M, Dober B, Duell CJ, Duff S, Duivenvoorden A, Dunkley J, Dusatko J, Errard J, Fabbian G, Feeney S, Ferraro S, Fluxà P, Freese K, Frisch JC, Frolov A, Fuller G, Fuzia B, Galitzki N, Gallardo PA, Tomas Galvez Ghersi J, Gao J, Gawiser E, Gerbino M, Gluscevic V, Goeckner-Wald N, Golec J, Gordon S, Gralla M, Green D, Grigorian A, Groh J, Groppi C, Guan Y, Gudmundsson JE, Han D, Hargrave P, Hasegawa M, Hasselfield M, Hattori M, Haynes V, Hazumi M, He Y, Healy E, Henderson SW, Hervias-Caimapo C, Hill CA, Hill JC, Hilton G, Hilton M, Hincks AD, Hinshaw G, Hložek R, Ho S, Ho SPP, Howe L, Huang Z, Hubmayr J, Huppenberger K, Hughes JP, Ilias A, Ikape N, Irwin K, Jaffe AH, Jain B, Jeong O, Kaneko D, Karpel ED, Katayama N, Keating B, Kernasovskiy SS, Keskitalo R, Kisner T, Kiuchi K, Klein J, Knowles K, Koopman B, Kosowsky A, Krachmalnicoff N, Kuenstner SE, Kuo CL, Kusaka A, Lashner J, Lee A, Lee E, Leon D, Leung JSY, Lewis A, Li Y, Li Z, Limon M, Linder E, Lopez-Caraballo C, Louis T, Lowry L, Lungu M, Madhavacheril M, Mak D, Maldonado F, Mani H, Mates B, Matsuda F, Maurin L, Mauskopf P, May A, McCallum N, McKenney C, McMahon J, Meerburg PD, Meyers J, Miller A, Mirmelstein M, Moodley K, Munchmeyer M, Munson C, Naess S, Nati F, Navaroli M, Newburgh L, Nguyen HN, Niemack M, Nishino H, Orlowski-Scherer J, Page L, Partridge B, Peloton J, Perrotta F, Piccirillo L, Pisano G, Poletti D, Puddu R, Puglisi G, Raum C, Reichardt CL, Remazeilles M, Rephaeli Y, Riechers D, Rojas F, Roy A, Sadeh S, Sakurai Y, Salatino M, Sathyanarayana Rao M, Schaan E, Schmittfull M, Sehgal N, Seibert J, Seljak U, Sherwin B, Shimon M, Sierra C, Sievers J, Sikhosana P, Silva-Feaver M, Simon SM, Sinclair A, Siritanasak P, Smith K, Smith SR, Spergel D, Staggs ST, Stein G, Stevens JR, Stompor R, Suzuki A, Tajima O, Takakura S, Teply G, Thomas DB, Thorne B, Thornton R, Trac H, Tsai C, Tucker C, Ullom J, Vagnozzi S, van Engelen A, Van Lanen J, Van Winkle DD, Vavagiakis EM, Vergès C, Vissers M, Wagoner K, Walker S, Ward J, Westbrook B, Whitehorn N, Williams J, Williams J, Wollack EJ, Xu Z, Yu B, Yu C, Zago F, Zhang H, Zhu N and Simons Observatory Collaboration (2019), Feb. The Simons Observatory: science goals and forecasts. *Journal of Cosmology and Astroparticle Physics* 2019 (2), 056. doi:10.1088/1475-7516/2019/02/056. 1808.07445.
- Adelberger KL, Steidel CC, Shapley AE and Pettini M (2003), Feb. Galaxies and Intergalactic Matter at Redshift $z \sim 3$: Overview. *The Astrophysical Journal* 584 (1): 45–75. doi:10.1086/345660. astro-ph/0210314.
- Adelberger KL, Shapley AE, Steidel CC, Pettini M, Erb DK and Reddy NA (2005), Aug. The Connection between Galaxies and Intergalactic Absorption Lines at Redshift $2 \leq z \leq 3$. *The Astrophysical Journal* 629 (2): 636–653. doi:10.1086/431753. astro-ph/0505122.
- Altay G, Theuns T, Schaye J, Crighton NHM and Dalla Vecchia C (2011), Aug. Through Thick and Thin—H I Absorption in Cosmological Simulations. *The Astrophysical Journal Letters* 737 (2): L37. doi:10.1088/2041-8205/737/2/L37. 1012.4014.
- Amodeo S, Battaglia N, Schaan E, Ferraro S, Moser E, Aiola S, Austermann JE, Beall JA, Bean R, Becker DT, Bond RJ, Calabrese E, Calafut V, Choi SK, Denison EV, Devlin M, Duff SM, Duivenvoorden AJ, Dunkley J, Dünner R, Gallardo PA, Hall KR, Han D, Hill JC, Hilton GC, Hilton M, Hložek R, Hubmayr J, Huppenberger KM, Hughes JP, Koopman BJ, MacInnis A, McMahon J, Madhavacheril MS, Moodley K, Mroczkowski T, Naess S, Nati F, Newburgh LB, Niemack MD, Page LA, Partridge B, Schillaci A, Sehgal N, Sifón C, Spergel DN, Staggs S, Storer ER, Ullom JN, Vale LR, van Engelen A, Van Lanen J, Vavagiakis EM, Wollack EJ and Xu Z (2021), Mar. Atacama Cosmology Telescope: Modeling the gas thermodynamics in BOSS CMASS galaxies from kinematic and thermal Sunyaev-Zel'dovich measurements. *Physical Review D* 103 (6), 063514. doi:10.1103/PhysRevD.103.063514. 2009.05558.
- Aracil B, Petitjean P, Pichon C and Bergeron J (2004), Jun. Metals in the intergalactic medium. *Astronomy and Astrophysics* 419: 811–819. doi:10.1051/0004-6361:20034346. astro-ph/0307506.
- Artale MC, Haider M, Montero-Dorta AD, Vogelsberger M, Martizzi D, Torrey P, Bird S, Hernquist L and Marinacci F (2022), Feb. The large-scale distribution of ionized metals in IllustrisTNG. *Monthly Notices of the Royal Astronomical Society* 510 (1): 399–412. doi:10.1093/mnras/stab3281. 2102.01092.
- Bahcall JN and Peebles PJE (1969), Apr. Statistical Tests for the Origin of Absorption Lines Observed in Quasi-Stellar Sources. *The Astrophysical Journal Letters* 156: L7. doi:10.1086/180337.
- Bahcall JN and Salpeter EE (1965), Nov. On the Interaction of Radiation from Distant Sources with the Intervening Medium. *The Astrophysical Journal* 142: 1677–1680. doi:10.1086/148460.

- Baker JG and Menzel DH (1938), Jul. Physical Processes in Gaseous Nebulae. III. The Balmer Decrement. *The Astrophysical Journal* 88: 52. doi:10.1086/143959.
- Becker GD, Hewett PC, Worseck G and Prochaska JX (2013), Apr. A refined measurement of the mean transmitted flux in the Ly α forest over $2 < z < 5$ using composite quasar spectra. *Monthly Notices of the Royal Astronomical Society* 430 (3): 2067–2081. doi:10.1093/mnras/stt031.1208.2584.
- Bond JR, Kofman L and Pogosyan D (1996), Apr. How filaments of galaxies are woven into the cosmic web. *Nature* 380 (6575): 603–606. doi:10.1038/380603a0. astro-ph/9512141.
- Bregman JN (2007), Sep. The Search for the Missing Baryons at Low Redshift. *Annual Review of Astronomy and Astrophysics* 45 (1): 221–259. doi:10.1146/annurev.astro.45.051806.110619.0706.1787.
- Burbidge EM, Lynds CR and Burbidge GR (1966), Apr. ON the Measurement and Interpretation of Absorption Features in the Spectrum of the Quasi-Stellar Object 3c 191. *The Astrophysical Journal* 144: 447. doi:10.1086/148629.
- Burchett JN, Tripp TM, Prochaska JX, Werk JK, Tumlinson J, Howk JC, Willmer CNA, Lehner N, Meiring JD, Bowen DV, Bordoloi R, Peebles MS, Jenkins EB, O'Meara JM, Tejos N and Katz N (2019), Jun. The COS Absorption Survey of Baryon Harbors (CASBaH): Warm-Hot Circumgalactic Gas Reservoirs Traced by Ne VIII Absorption. *The Astrophysical Journal Letters* 877 (2), L20. doi:10.3847/2041-8213/ab1f7f.1810.06560.
- Burchett JN, Elek O, Tejos N, Prochaska JX, Tripp TM, Bordoloi R and Forbes AG (2020), Mar. Revealing the Dark Threads of the Cosmic Web. *The Astrophysical Journal Letters* 891 (2), L35. doi:10.3847/2041-8213/ab700c.2003.04393.
- Cantalupo S, Arrigoni-Battaia F, Prochaska JX, Hennawi JF and Madau P (2014), Feb. A cosmic web filament revealed in Lyman- α emission around a luminous high-redshift quasar. *Nature* 506 (7486): 63–66. doi:10.1038/nature12898.1401.4469.
- Carswell RF and Webb JK (2014), Aug. VPFIT: Voigt profile fitting program. Astrophysics Source Code Library, record ascl:1408.015.
- Cen R and Ostriker JP (1999), Mar. Where Are the Baryons? *The Astrophysical Journal* 514 (1): 1–6. doi:10.1086/306949. astro-ph/9806281.
- Cen R and Ostriker JP (2006), Oct. Where Are the Baryons? II. Feedback Effects. *The Astrophysical Journal* 650 (2): 560–572. doi:10.1086/506505. astro-ph/0601008.
- Charlton J and Churchill C (2000), Quasistellar Objects: Intervening Absorption Lines, Murdin P, (Ed.), Encyclopedia of Astronomy and Astrophysics, pp. 2366.
- Chen HW, Prochaska JX, Weiner BJ, Mulchaey JS and Williger GM (2005), Aug. Probing the Intergalactic Medium-Galaxy Connection toward PKS 0405-123. II. A Cross-Correlation Study of Ly α Absorbers and Galaxies at $z > 0.5$. *The Astrophysical Journal Letters* 629 (1): L25–L28. doi:10.1086/444377. astro-ph/0507621.
- Cordes JM and Chatterjee S (2019), Aug. Fast Radio Bursts: An Extragalactic Enigma. *Annual Review of Astronomy and Astrophysics* 57: 417–465. doi:10.1146/annurev-astro-091918-104501.1906.05878.
- Croft RAC, Weinberg DH, Katz N and Hernquist L (1998), Mar. Recovery of the Power Spectrum of Mass Fluctuations from Observations of the Ly α Forest. *The Astrophysical Journal* 495 (1): 44–62. doi:10.1086/305289. astro-ph/9708018.
- Cybert RH, Fields BD, Olive KA and Yeh TH (2016), Jan. Big bang nucleosynthesis: Present status. *Reviews of Modern Physics* 88 (1), 015004. doi:10.1103/RevModPhys.88.015004.1505.01076.
- Danforth CW, Stocke JT and Shull JM (2010), Feb. Broad H I Absorbers as Metallicity-independent Tracers of the Warm-Hot Intergalactic Medium. *The Astrophysical Journal* 710 (1): 613–633. doi:10.1088/0004-637X/710/1/613.0912.1603.
- Danforth CW, Keeney BA, Tilton EM, Shull JM, Stocke JT, Stevans M, Pieri MM, Savage BD, France K, Syphers D, Smith BD, Green JC, Froning C, Penton SV and Osterman SN (2016), Feb. An HST/COS Survey of the Low-redshift Intergalactic Medium. I. Survey, Methodology, and Overall Results. *The Astrophysical Journal* 817 (2), 111. doi:10.3847/0004-637X/817/2/111.1402.2655.
- Davé R, Cen R, Ostriker JP, Bryan GL, Hernquist L, Katz N, Weinberg DH, Norman ML and O'Shea B (2001), May. Baryons in the Warm-Hot Intergalactic Medium. *The Astrophysical Journal* 552 (2): 473–483. doi:10.1086/320548. astro-ph/0007217.
- Davé R, Oppenheimer BD, Katz N, Kollmeier JA and Weinberg DH (2010), Nov. The intergalactic medium over the last 10 billion years - I. Ly α absorption and physical conditions. *Monthly Notices of the Royal Astronomical Society* 408 (4): 2051–2070. doi:10.1111/j.1365-2966.2010.17279.x.1005.2421.
- de Graaff A, Cai YC, Heymans C and Peacock JA (2019), Apr. Probing the missing baryons with the Sunyaev-Zel'dovich effect from filaments. *Astronomy and Astrophysics* 624, A48. doi:10.1051/0004-6361/201935159.1709.10378.
- Dekel A and Birnboim Y (2006), May. Galaxy bimodality due to cold flows and shock heating. *Monthly Notices of the Royal Astronomical Society* 368 (1): 2–20. doi:10.1111/j.1365-2966.2006.10145.x. astro-ph/0412300.
- Dinshaw N, Impey CD, Foltz CB, Weymann RJ and Chaffee FH (1994), Dec. Common Lyman-Alpha Absorption toward the Quasar Pair Q1343+2640A, B: Evidence for Large and Quiescent Clouds. *The Astrophysical Journal Letters* 437: L87. doi:10.1086/187689.
- D'Odorico V, Cristiani S, Pomante E, Carswell RF, Viel M, Barai P, Becker GD, Calura F, Cupani G, Fontanot F, Haehnelt MG, Kim TS, Miralda-Escudé J, Rorai A, Tescari E and Vanzella E (2016), Dec. Metals in the $z \sim 3$ intergalactic medium: results from an ultra-high signal-to-noise ratio UVES quasar spectrum. *Monthly Notices of the Royal Astronomical Society* 463 (3): 2690–2707. doi:10.1093/mnras/stw2161.1608.06116.
- Draine BT (2011). Physics of the Interstellar and Intergalactic Medium.
- Ellison SL, Songaila A, Schaye J and Pettini M (2000), Sep. The Enrichment History of the Intergalactic Medium-Measuring the C IV/H I Ratio in the Ly α Forest. *The Astronomical Journal* 120 (3): 1175–1191. doi:10.1086/301511. astro-ph/0005448.
- Fan X, Strauss MA, Becker RH, White RL, Gunn JE, Knapp GR, Richards GT, Schneider DP, Brinkmann J and Fukugita M (2006), Jul. Constraining the Evolution of the Ionizing Background and the Epoch of Reionization with $z \sim 6$ Quasars. II. A Sample of 19 Quasars. *The Astronomical Journal* 132 (1): 117–136. doi:10.1086/504836. astro-ph/0512082.
- Fan X, Bañados E and Simcoe RA (2023), Aug. Quasars and the Intergalactic Medium at Cosmic Dawn. *Annual Review of Astronomy and Astrophysics* 61: 373–426. doi:10.1146/annurev-astro-052920-102455.2212.06907.
- Fang Y, Duncan RC, Crofts APS and Bechtold J (1996), May. The Size and Nature of Lyman- α Forest Clouds Probed by QSO Pairs and Groups. *The Astrophysical Journal* 462: 77. doi:10.1086/177129. astro-ph/9510112.
- Faucher-Giguère CA and Oh SP (2023), Aug. Key Physical Processes in the Circumgalactic Medium. *Annual Review of Astronomy and Astrophysics* 61: 131–195. doi:10.1146/annurev-astro-052920-125203.2301.10253.
- Ferland GJ, Korista KT, Verner DA, Ferguson JW, Kingdon JB and Verner EM (1998), Jul. CLOUDY 90: Numerical Simulation of Plasmas and Their Spectra. *Publications of the Astronomical Society of the Pacific* 110 (749): 761–778. doi:10.1086/316190.
- Fields BD, Olive KA, Yeh TH and Young C (2020), Mar. Big-Bang Nucleosynthesis after Planck. *Journal of Cosmology and Astroparticle Physics* 2020 (3), 010. doi:10.1088/1475-7516/2020/03/010.1912.01132.
- Fukugita M, Hogan CJ and Peebles PJE (1998), Aug. The Cosmic Baryon Budget. *The Astrophysical Journal* 503 (2): 518–530. doi:10.1086/306025. astro-ph/9712020.
- Fumagalli M, Prochaska JX, Kasen D, Dekel A, Ceverino D and Primack JR (2011), Dec. Absorption-line systems in simulated galaxies fed by cold streams. *Monthly Notices of the Royal Astronomical Society* 418 (3): 1796–1821. doi:10.1111/j.1365-2966.2011.19599.x.1103.2130.

- Galárraga-Espinosa D, Aghanim N, Langer M and Tanimura H (2021), May. Properties of gas phases around cosmic filaments at $z = 0$ in the IllustrisTNG simulation. *Astronomy and Astrophysics* 649, A117. doi:10.1051/0004-6361/202039781. 2010.15139.
- Gallego SG, Cantalupo S, Lilly S, Marino RA, Pezzulli G, Schaye J, Wisotzki L, Bacon R, Inami H, Akhlaghi M, Tacchella S, Richard J, Bouche NF, Steinmetz M and Carollo M (2018), Apr. Stacking the Cosmic Web in fluorescent Ly α emission with MUSE. *Monthly Notices of the Royal Astronomical Society* 475 (3): 3854–3869. doi:10.1093/mnras/sty037. 1706.03785.
- Gunn JE and Peterson BA (1965), Nov. On the Density of Neutral Hydrogen in Intergalactic Space. *The Astrophysical Journal* 142: 1633–1636. doi:10.1086/148444.
- Haardt F and Madau P (2012), Feb. Radiative Transfer in a Clumpy Universe. IV. New Synthesis Models of the Cosmic UV/X-Ray Background. *The Astrophysical Journal* 746 (2), 125. doi:10.1088/0004-637X/746/2/125. 1105.2039.
- Hernquist L, Katz N, Weinberg DH and Miralda-Escudé J (1996), Feb. The Lyman-Alpha Forest in the Cold Dark Matter Model. *The Astrophysical Journal Letters* 457: L51. doi:10.1086/309899. astro-ph/9509105.
- Hui L and Gnedin NY (1997), Nov. Equation of state of the photoionized intergalactic medium. *Monthly Notices of the Royal Astronomical Society* 292 (1): 27–42. doi:10.1093/mnras/292.1.27. astro-ph/9612232.
- Hummels CB, Smith BD and Silvia DW (2017), Sep. Trident: A Universal Tool for Generating Synthetic Absorption Spectra from Astrophysical Simulations. *The Astrophysical Journal* 847 (1), 59. doi:10.3847/1538-4357/aa7e2d. 1612.03935.
- Janknecht E, Reimers D, Lopez S and Tytler D (2006), Nov. The evolution of Lyman α absorbers in the redshift range $0.5 < z < 1.9$. *Astronomy and Astrophysics* 458 (2): 427–439. doi:10.1051/0004-6361/20065372. astro-ph/0608342.
- Japelj J, Laigle C, Puech M, Pichon C, Rahmani H, Dubois Y, Devriendt JEG, Petitjean P, Hammer F, Gendron E, Kaper L, Morris S, Pirzkal N, Sánchez-Janssen R, Slyz A, Vergani SD and Yang Y (2019), Dec. Simulating MOS science on the ELT: Ly α forest tomography. *Astronomy and Astrophysics* 632, A94. doi:10.1051/0004-6361/201936048. 1911.00021.
- Kereš D, Katz N, Weinberg DH and Davé R (2005), Oct. How do galaxies get their gas? *Monthly Notices of the Royal Astronomical Society* 363 (1): 2–28. doi:10.1111/j.1365-2966.2005.09451.x. astro-ph/0407095.
- Khaire V and Srianand R (2019), Apr. New synthesis models of consistent extragalactic background light over cosmic time. *Monthly Notices of the Royal Astronomical Society* 484 (3): 4174–4199. doi:10.1093/mnras/stz174. 1801.09693.
- Khyrkis IS, Ata M, Lee KG, Simha S, Huang Y, Prochaska JX, Tejos N, Bannister KW, Cooke J, Day CK, Deller A, Glowacki M, Gordon AC, James CW, Marnoch L, Shannon RM, Zhang J and Bernal-Cortes L (2024), Oct. FLIMFLAM DR1: The First Constraints on the Cosmic Baryon Distribution from Eight Fast Radio Burst Sight Lines. *The Astrophysical Journal* 973 (2), 151. doi:10.3847/1538-4357/ad6567. 2402.00505.
- Kim TS, Cristiani S and D’Odorico S (2001), Jul. The Ly α forest at $1.5 < z < 4$. *Astronomy and Astrophysics* 373: 757–781. doi:10.1051/0004-6361:20010650. astro-ph/0101005.
- Kim TS, Wakker BP, Nasir F, Carswell RF, Savage BD, Bolton JS, Fox AJ, Viel M, Haehnelt MG, Charlton JC and Rosenwasser BE (2021), Mar. The evolution of the low-density H I λ intergalactic medium from $z = 3.6$ to 0: data, transmitted flux, and H I λ column density. *Monthly Notices of the Royal Astronomical Society* 501 (4): 5811–5833. doi:10.1093/mnras/staa3844. 2012.05861.
- Lanzetta KM, Wolfe AM and Turnshek DA (1995), Feb. The IUE Survey for Damped Lyman- α and Lyman-Limit Absorption Systems: Evolution of the Gaseous Content of the Universe. *The Astrophysical Journal* 440: 435. doi:10.1086/175286.
- Lee KG, Krolewski A, White M, Schlegel D, Nugent PE, Hennawi JF, Müller T, Pan R, Prochaska JX, Font-Ribera A, Suzuki N, Glazebrook K, Kacprzak GG, Kartaltepe JS, Koekemoer AM, Le Fèvre O, Lemaux BC, Maier C, Nanayakkara T, Rich RM, Sanders DB, Salvato M, Tasca L and Tran KVV (2018), Aug. First Data Release of the COSMOS Ly α Mapping and Tomography Observations: 3D Ly α Forest Tomography at $2.05 < z < 2.55$. *The Astrophysical Journal Supplement Series* 237 (2), 31. doi:10.3847/1538-4365/aace58. 1710.02894.
- Lehner N, Savage BD, Richter P, Sembach KR, Tripp TM and Wakker BP (2007), Apr. Physical Properties, Baryon Content, and Evolution of the Ly α Forest: New Insights from High-Resolution Observations at $z < 0.4$. *The Astrophysical Journal* 658 (2): 680–709. doi:10.1086/511749. astro-ph/0612275.
- Lehner N, Howk JC, Tripp TM, Tumlinson J, Prochaska JX, O’Meara JM, Thom C, Werk JK, Fox AJ and Ribaldo J (2013), Jun. The Bimodal Metallicity Distribution of the Cool Circumgalactic Medium at $z < 1$. *The Astrophysical Journal* 770 (2), 138. doi:10.1088/0004-637X/770/2/138. 1302.5424.
- Lidz A, Faucher-Giguère CA, Dall’Aglio A, McQuinn M, Fechner C, Zaldarriaga M, Hernquist L and Dutta S (2010), Jul. A Measurement of Small-scale Structure in the $2.2 < z < 4.2$ Ly α Forest. *The Astrophysical Journal* 718 (1): 199–230. doi:10.1088/0004-637X/718/1/199. 0909.5210.
- Lopez S, Tejos N, Ledoux C, Barrientos LF, Sharon K, Rigby JR, Gladders MD, Bayliss MB and Pessa I (2018), Feb. A clumpy and anisotropic galaxy halo at redshift 1 from gravitational-arc tomography. *Nature* 554 (7693): 493–496. doi:10.1038/nature25436. 1801.10175.
- Lorimer DR, Bailes M, McLaughlin MA, Narkevic DJ and Crawford F (2007), Nov. A Bright Millisecond Radio Burst of Extragalactic Origin. *Science* 318 (5851): 777. doi:10.1126/science.1147532. 0709.4301.
- Lynds R (1971), Mar. The Absorption-Line Spectrum of 4c 05.34. *The Astrophysical Journal Letters* 164: L73. doi:10.1086/180695.
- Macquart JP, Prochaska JX, McQuinn M, Bannister KW, Bhandari S, Day CK, Deller AT, Ekers RD, James CW, Marnoch L, Osłowski S, Phillips C, Ryder SD, Scott DR, Shannon RM and Tejos N (2020), May. A census of baryons in the Universe from localized fast radio bursts. *Nature* 581 (7809): 391–395. doi:10.1038/s41586-020-2300-2. 2005.13161.
- Marra R, Churchill CW, Kacprzak GG, Nielsen NM, Trujillo-Gomez S and Lewis EA (2024), Feb. Examining quasar absorption-line analysis methods: the tension between simulations and observational assumptions key to modelling clouds. *Monthly Notices of the Royal Astronomical Society* 527 (4): 10522–10537. doi:10.1093/mnras/stad3735. 2202.12228.
- Martizzi D, Vogelsberger M, Artales MC, Haider M, Torrey P, Marinacci F, Nelson D, Pillepich A, Weinberger R, Hernquist L, Naiman J and Springel V (2019), Jul. Baryons in the Cosmic Web of IllustrisTNG - I: gas in knots, filaments, sheets, and voids. *Monthly Notices of the Royal Astronomical Society* 486 (3): 3766–3787. doi:10.1093/mnras/stz1106. 1810.01883.
- McDonald P, Seljak U, Cen R, Shih D, Weinberg DH, Burles S, Schneider DP, Schlegel DJ, Bahcall NA, Briggs JW, Brinkmann J, Fukugita M, Ivezić Z, Kent S and Vanden Berk DE (2005), Dec. The Linear Theory Power Spectrum from the Ly α Forest in the Sloan Digital Sky Survey. *The Astrophysical Journal* 635 (2): 761–783. doi:10.1086/497563. astro-ph/0407377.
- McQuinn M (2016), Sep. The Evolution of the Intergalactic Medium. *Annual Review of Astronomy and Astrophysics* 54: 313–362. doi:10.1146/annurev-astro-082214-122355. 1512.00086.
- McQuinn M and O’Donoghue PR (2016), Feb. On the intergalactic temperature-density relation. *Monthly Notices of the Royal Astronomical Society* 456 (1): 47–54. doi:10.1093/mnras/stv2675. 1505.07875.
- McQuinn M, Oh SP and Faucher-Giguère CA (2011), Dec. On Lyman-limit Systems and the Evolution of the Intergalactic Ionizing Background. *The Astrophysical Journal* 743 (1), 82. doi:10.1088/0004-637X/743/1/82. 1101.1964.
- Meiksin AA (2009), Oct. The physics of the intergalactic medium. *Reviews of Modern Physics* 81 (4): 1405–1469. doi:10.1103/RevModPhys.81.1405. 0711.3358.
- Merloni A, Lamer G, Liu T, Ramos-Ceja ME, Brunner H, Bulbul E, Dennerl K, Doroshenko V, Freyberg MJ, Friedrich S, Gatuzz E, Georgakakis A, Haberl F, Igo Z, Kreykenbohm I, Liu A, Maitra C, Malyali A, Mayer MGF, Nandra K, Predehl P, Robrade J, Salvato M, Sanders JS, Stewart

- I, Tubín-Arenas D, Weber P, Wilms J, Arcodia R, Artis E, Aschersleben J, Avakyan A, Aydar C, Bahar YE, Balzer F, Becker W, Berger K, Boller T, Bornemann W, Brüggen M, Brusa M, Buchner J, Burwitz V, Camilloni F, Clerc N, Comparat J, Coutinho D, Czesla S, Dannhauer SM, Dauner L, Dauser T, Dietl J, Dolag K, Dwelly T, Egg K, Ehl E, Freund S, Friedrich P, Gaida R, Garrel C, Ghirardini V, Gokus A, Grünwald G, Grandis S, Grotova I, Gruen D, Gueguen S, Hämmerich S, Hamaus N, Hasinger G, Haubner K, Homan D, Ider Chitham J, Joseph WM, Joyce A, König O, Kaltenbrunner DM, Khokhriakova A, Kink W, Kirsch C, Kluge M, Knies J, Krippendorf S, Krümpe M, Kurpas J, Li P, Liu Z, Locatelli N, Lorenz M, Müller S, Magaudda E, Mannes C, McCall H, Meidinger N, Michailidis M, Migkas K, Muñoz-Giraldo D, Musiimenta B, Nguyen-Dang NT, Ni Q, Olechowska A, Ota N, Pacaud F, Pasini T, Perinati E, Pires AM, Pommranz C, Ponti G, Poppenhaeager K, Pühlhofer G, Rau A, Reh M, Reiprich TH, Roster W, Saeedi S, Santangelo A, Sasaki M, Schmitt J, Schneider PC, Schrabback T, Schuster N, Schwöpe A, Seppi R, Serim MM, Shreeram S, Sokolova-Lapa E, Starck H, Stelzer B, Stierhof J, Suleimanov V, Tenzer C, Traulsen I, Trümper J, Tsuge K, Urrutia T, Veronica A, Waddell SGH, Willer R, Wolf J, Yeung MCH, Zainab A, Zangrandi F, Zhang X, Zhang Y and Zheng X (2024), Feb. The SRG/eROSITA all-sky survey. First X-ray catalogues and data release of the western Galactic hemisphere. *Astronomy and Astrophysics* 682, A34. doi:10.1051/0004-6361/202347165. 2401.17274.
- Miralda-Escudé J and Rees MJ (1994), Jan. Reionization and thermal evolution of a photoionized intergalactic medium. *Monthly Notices of the Royal Astronomical Society* 266: 343–352. doi:10.1093/mnras/266.2.343.
- Mo H, van den Bosch FC and White S (2010). Galaxy Formation and Evolution.
- Morris SL, Weymann RJ, Dressler A, McCarthy PJ, Smith BA, Terrielle RJ, Giovanelli R and Irwin M (1993), Dec. The Environment of Lyman-alpha Absorbers in the Sight Line toward 3C 273. *The Astrophysical Journal* 419: 524. doi:10.1086/173505. astro-ph/9307005.
- Morton DC (2003), Nov. Atomic Data for Resonance Absorption Lines. III. Wavelengths Longward of the Lyman Limit for the Elements Hydrogen to Gallium. *The Astrophysical Journal Supplement Series* 149 (1): 205–238. doi:10.1086/377639.
- Nelson D, Springel V, Pillepich A, Rodriguez-Gomez V, Torrey P, Genel S, Vogelsberger M, Pakmor R, Marinacci F, Weinberger R, Kelley L, Lovell M, Diemer B and Hernquist L (2019), May. The IllustrisTNG simulations: public data release. *Computational Astrophysics and Cosmology* 6 (1), 2. doi:10.1186/s40668-019-0028-x. 1812.05609.
- Nicastro F, Kaastra J, Krongold Y, Borgani S, Branchini E, Cen R, Dadina M, Danforth CW, Elvis M, Fiore F, Gupta A, Mathur S, Mayya D, Paerels F, Piro L, Rosa-Gonzalez D, Schaye J, Shull JM, Torres-Zafra J, Wijers N and Zappacosta L (2018), Jun. Observations of the missing baryons in the warm-hot intergalactic medium. *Nature* 558 (7710): 406–409. doi:10.1038/s41586-018-0204-1. 1806.08395.
- Oppenheimer BD and Davé R (2006), Dec. Cosmological simulations of intergalactic medium enrichment from galactic outflows. *Monthly Notices of the Royal Astronomical Society* 373 (4): 1265–1292. doi:10.1111/j.1365-2966.2006.10989.x. astro-ph/0605651.
- Pakmor R, Springel V, Coles JP, Guillet T, Pfrommer C, Bose S, Barrera M, Delgado AM, Ferlito F, Frenk C, Hadzhiyska B, Hernández-Aguayo C, Hernquist L, Kannan R and White SDM (2023), Sep. The MillenniumTNG Project: the hydrodynamical full physics simulation and a first look at its galaxy clusters. *Monthly Notices of the Royal Astronomical Society* 524 (2): 2539–2555. doi:10.1093/mnras/stac3620. 2210.10060.
- Peebles PJE (1974), Apr. The Gravitational-Instability Picture and the Nature of the Distribution of Galaxies. *The Astrophysical Journal Letters* 189: L51. doi:10.1086/181462.
- Penton SV, Stocke JT and Shull JM (2002), Feb. The Local Ly α Forest. III. Relationship between Ly α Absorbers and Galaxies, Voids, and Superclusters. *The Astrophysical Journal* 565 (2): 720–742. doi:10.1086/324483. astro-ph/0109277.
- Péroux C and Howk JC (2020), Aug. The Cosmic Baryon and Metal Cycles. *Annual Review of Astronomy and Astrophysics* 58: 363–406. doi:10.1146/annurev-astro-021820-120014. 2011.01935.
- Planck Collaboration, Aghanim N, Akrami Y, Ashdown M, Aumont J, Baccigalupi C, Ballardini M, Banday AJ, Barreiro RB, Bartolo N, Basak S, Battye R, Benabed K, Bernard JP, Bersanelli M, Bielewicz P, Bock JJ, Bond JR, Borrill J, Bouchet FR, Boulanger F, Bucher M, Burigana C, Butler RC, Calabrese E, Cardoso JF, Carron J, Challinor A, Chiang HC, Chluba J, Colombo LPL, Combet C, Contreras D, Crill BP, Cuttaia F, de Bernardis P, de Zotti G, Delabrouille J, Delouis JM, Di Valentino E, Diego JM, Doré O, Douspis M, Ducout A, Dupac X, Dusini S, Efstathiou G, Elsner F, Enßlin TA, Eriksen HK, Fantaye Y, Farhang M, Fergusson J, Fernandez-Cobos R, Finelli F, Forastieri F, Frailis M, Fraisse AA, Franceschi E, Frolov A, Galeotta S, Galli S, Ganga K, Génova-Santos RT, Gerbino M, Ghosh T, González-Nuevo J, Górski KM, Gratton S, Gruppuso A, Gudmundsson JE, Hamann J, Handley W, Hansen FK, Herranz D, Hildebrandt SR, Hivon E, Huang Z, Jaffe AH, Jones WC, Karakci A, Keihänen E, Keskitalo R, Kiiveri K, Kim J, Kisner TS, Knox L, Krachmalnicoff N, Kunz M, Kurki-Suonio H, Lagache G, Lamarre JM, Lasenby A, Lattanzi M, Lawrence CR, Le Jeune M, Lemos P, Lesgourgues J, Levrier F, Lewis A, Liguori M, Lilje PB, Lilley M, Lindholm V, López-Cañiego M, Lubin PM, Ma YZ, Macías-Pérez JF, Maggio G, Maino D, Mandolesi N, Mangilli A, Marcos-Caballero A, Maris M, Martin PG, Martinelli M, Martínez-González E, Matarrese S, Mauri N, McEwen JD, Meinhold PR, Melchiorri A, Mennella A, Migliaccio M, Millea M, Mitra S, Miville-Deschênes MA, Molinari D, Montier L, Morgante G, Moss A, Natoli P, Nørgaard-Nielsen HU, Pagano L, Paoletti D, Partridge B, Patanchon G, Peiris HV, Perrotta F, Pettorino V, Piacentini F, Polastri L, Polenta G, Puget JL, Rachen JP, Reinecke M, Remazeilles M, Renzi A, Rocha G, Rosset C, Roudier G, Rubiño-Martín JA, Ruiz-Granados B, Salvati L, Sandri M, Savelainen M, Scott D, Shellard EPS, Sirignano C, Sirri G, Spencer LD, Sunyaev R, Suur-Uski AS, Tauber JA, Tavagnacco D, Tenti M, Toffolatti L, Tomasi M, Trombetti T, Valenziano L, Valiviita J, Van Tent B, Vibert L, Vielva P, Villa F, Vittorio N, Wandelt BD, Wehus IK, White M, White SDM, Zacchei A and Zonca A (2020), Sep. Planck 2018 results. VI. Cosmological parameters. *Astronomy and Astrophysics* 641, A6. doi:10.1051/0004-6361/201833910. 1807.06209.
- Press WH and Schechter P (1974), Feb. Formation of Galaxies and Clusters of Galaxies by Self-Similar Gravitational Condensation. *The Astrophysical Journal* 187: 425–438. doi:10.1086/152650.
- Prochaska JX, O'Meara JM and Worseck G (2010), Jul. A Definitive Survey for Lyman Limit Systems at $z \sim 3.5$ with the Sloan Digital Sky Survey. *The Astrophysical Journal* 718 (1): 392–416. doi:10.1088/0004-637X/718/1/392. 0912.0292.
- Prochaska JX, Weiner B, Chen HW, Mulchaey J and Cooksey K (2011), Oct. Probing the Intergalactic Medium/Galaxy Connection. V. On the Origin of Ly α and O VI Absorption at $z \sim 0.2$. *The Astrophysical Journal* 740 (2), 91. doi:10.1088/0004-637X/740/2/91. 1103.1891.
- Prochaska JX, Tejos N, Crighton N, Jnburchett, Tiffanyhsy, Tuo-Ji, Marijana777, Ktirimba, Jhennawi, Cooke R, O'Meara J and Werk J (2017), Oct. linetools/linetools: Third Minor Release. doi:10.5281/zenodo.1036773.
- Rauch M (1998), Jan. The Lyman Alpha Forest in the Spectra of QSOs. *Annual Review of Astronomy and Astrophysics* 36: 267–316. doi:10.1146/annurev-astro.36.1.267. astro-ph/9806286.
- Rauch M, Becker GD, Viel M, Sargent WLW, Smette A, Simcoe RA, Barlow TA and Haehnelt MG (2005), Oct. Expansion and Collapse in the Cosmic Web. *The Astrophysical Journal* 632 (1): 58–80. doi:10.1086/432904. astro-ph/0509262.
- Richter P, Savage BD, Sembach KR and Tripp TM (2006), Jan. Tracing baryons in the warm-hot intergalactic medium with broad Ly α absorption. *Astronomy and Astrophysics* 445 (3): 827–842. doi:10.1051/0004-6361:20053636. astro-ph/0509539.
- Robertson BE (2022), Aug. Galaxy Formation and Reionization: Key Unknowns and Expected Breakthroughs by the James Webb Space Telescope. *Annual Review of Astronomy and Astrophysics* 60: 121–158. doi:10.1146/annurev-astro-120221-044656. 2110.13160.
- Rorai A, Hennawi JF and White M (2013), Oct. A New Method to Directly Measure the Jeans Scale of the Intergalactic Medium Using Close Quasar Pairs. *The Astrophysical Journal* 775 (2), 81. doi:10.1088/0004-637X/775/2/81. 1305.0210.
- Rudie GC, Steidel CC, Trainor RF, Rakic O, Bogosavljević M, Pettini M, Reddy N, Shapley AE, Erb DK and Law DR (2012), May. The Gaseous Environment of High- z Galaxies: Precision Measurements of Neutral Hydrogen in the Circumgalactic Medium of $z \sim 2$ –3 Galaxies in the Keck

- Baryonic Structure Survey. *The Astrophysical Journal* 750 (1), 67. doi:10.1088/0004-637X/750/1/67. 1202.6055.
- Salvaterra R, Della Valle M, Campana S, Chincarini G, Covino S, D'Avanzo P, Fernández-Soto A, Guidorzi C, Mannucci F, Margutti R, Thöne CC, Antonelli LA, Barthelmy SD, de Pasquale M, D'Elia V, Fiore F, Fugazza D, Hunt LK, Maiorano E, Marinoni S, Marshall FE, Molinari E, Nousek J, Pian E, Racusin JL, Stella L, Amati L, Andreuzzi G, Cusumano G, Fenimore EE, Ferrero P, Giommi P, Guetta D, Holland ST, Hurley K, Israel GL, Mao J, Markwardt CB, Masetti N, Pagani C, Palazzi E, Palmer DM, Piranomonte S, Tagliaferri G and Testa V (2009), Oct. GRB090423 at a redshift of $z=8.1$. *Nature* 461 (7268): 1258–1260. doi:10.1038/nature08445. 0906.1578.
- Savage BD, Kim TS, Wakker BP, Keeney B, Shull JM, Stocke JT and Green JC (2014), May. The Properties of Low Redshift Intergalactic O VI Absorbers Determined from High S/N Observations of 14 QSOs with the Cosmic Origins Spectrograph. *The Astrophysical Journal Supplement Series* 212 (1), 8. doi:10.1088/0067-0049/212/1/8. 1403.7542.
- Scannapieco E, Ferrara A and Madau P (2002), Aug. Early Enrichment of the Intergalactic Medium and Its Feedback on Galaxy Formation. *The Astrophysical Journal* 574 (2): 590–598. doi:10.1086/341114. astro-ph/0201463.
- Schaye J (2001), Oct. Model-independent Insights into the Nature of the Ly α Forest and the Distribution of Matter in the Universe. *The Astrophysical Journal* 559 (2): 507–515. doi:10.1086/322421. astro-ph/0104272.
- Schaye J, Theuns T, Rauch M, Efstathiou G and Sargent WLW (2000), Nov. The thermal history of the intergalactic medium*. *Monthly Notices of the Royal Astronomical Society* 318 (3): 817–826. doi:10.1046/j.1365-8711.2000.03815.x. astro-ph/9912432.
- Schmidt M (1963), Mar. 3C 273 : A Star-Like Object with Large Red-Shift. *Nature* 197 (4872): 1040. doi:10.1038/1971040a0.
- Schmidt M (1965), Jan. Optical Spectra and Redshifts of 31 Radio Galaxies. *The Astrophysical Journal* 141: 1. doi:10.1086/148085.
- Shull JM, Smith BD and Danforth CW (2012), Nov. The Baryon Census in a Multiphase Intergalactic Medium: 30% of the Baryons May Still be Missing. *The Astrophysical Journal* 759 (1), 23. doi:10.1088/0004-637X/759/1/23. 1112.2706.
- Smette A, Robertson JG, Shaver PA, Reimers D, Wisotzki L and Koehler T (1995), Oct. The gravitational lens candidate HE 1104-1805 and the size of absorption systems. *Astronomy and Astrophysics Supplement Series* 113: 199.
- Somerville RS and Davé R (2015), Aug. Physical Models of Galaxy Formation in a Cosmological Framework. *Annual Review of Astronomy and Astrophysics* 53: 51–113. doi:10.1146/annurev-astro-082812-140951. 1412.2712.
- Songaila A and Cowie LL (2010), Oct. The Evolution of Lyman Limit Absorption Systems to Redshift Six. *The Astrophysical Journal* 721 (2): 1448–1466. doi:10.1088/0004-637X/721/2/1448. 1007.3262.
- Sunyaev RA and Zeldovich YB (1972), Nov. The Observations of Relic Radiation as a Test of the Nature of X-Ray Radiation from the Clusters of Galaxies. *Comments on Astrophysics and Space Physics* 4: 173.
- Tejos N, Morris SL, Crighton NHM, Theuns T, Altay G and Finn CW (2012), Sep. Large-scale structure in absorption: gas within and around galaxy voids. *Monthly Notices of the Royal Astronomical Society* 425 (1): 245–260. doi:10.1111/j.1365-2966.2012.21448.x. 1205.2697.
- Tejos N, Morris SL, Finn CW, Crighton NHM, Bechtold J, Jannuzi BT, Schaye J, Theuns T, Altay G, Le Fèvre O, Ryan-Weber E and Davé R (2014), Jan. On the connection between the intergalactic medium and galaxies: the H I-galaxy cross-correlation at $z \leq 1$. *Monthly Notices of the Royal Astronomical Society* 437 (3): 2017–2075. doi:10.1093/mnras/stt1844. 1309.5950.
- Tejos N, Prochaska JX, Crighton NHM, Morris SL, Werk JK, Theuns T, Padilla N, Bielby RM and Finn CW (2016), Jan. Towards the statistical detection of the warm-hot intergalactic medium in intercluster filaments of the cosmic web. *Monthly Notices of the Royal Astronomical Society* 455 (3): 2662–2697. doi:10.1093/mnras/stv2376. 1506.01031.
- Theuns T, Leonard A, Efstathiou G, Pearce FR and Thomas PA (1998), Dec. P Λ SPH simulations of the Ly α forest. *Monthly Notices of the Royal Astronomical Society* 301 (2): 478–502. doi:10.1046/j.1365-8711.1998.02040.x. astro-ph/9805119.
- Theuns T, Viel M, Kay S, Schaye J, Carswell RF and Tzanavaris P (2002), Oct. Galactic Winds in the Intergalactic Medium. *The Astrophysical Journal Letters* 578 (1): L5–L8. doi:10.1086/344521. astro-ph/0208418.
- Tripp TM, Sembach KR, Bowen DV, Savage BD, Jenkins EB, Lehner N and Richter P (2008), Jul. A High-Resolution Survey of Low-Redshift QSO Absorption Lines: Statistics and Physical Conditions of O VI Absorbers. *The Astrophysical Journal Supplement Series* 177 (1): 39–102. doi:10.1086/587486. 0706.1214.
- Tumlinson J, Peebles MS and Werk JK (2017), Aug. The Circumgalactic Medium. *Annual Review of Astronomy and Astrophysics* 55 (1): 389–432. doi:10.1146/annurev-astro-091916-055240. 1709.09180.
- Tytler D (1982), Jul. QSO Lyman limit absorption. *Nature* 298 (5873): 427–432. doi:10.1038/298427a0.
- Upton Sanderbeck PR, D'Aloisio A and McQuinn MJ (2016), Aug. Models of the thermal evolution of the intergalactic medium after reionization. *Monthly Notices of the Royal Astronomical Society* 460 (2): 1885–1897. doi:10.1093/mnras/stw1117. 1511.05992.
- van de Hulst HC and Reesinck JJM (1947), Jul. Line Breadths and Voigt Profiles. *The Astrophysical Journal* 106: 121. doi:10.1086/144944.
- Veilleux S, Maiolino R, Bolatto AD and Aalto S (2020), Apr. Cool outflows in galaxies and their implications. *The Astronomy and Astrophysics Review* 28 (1), 2. doi:10.1007/s00159-019-0121-9. 2002.07765.
- Verner DA, Barthel PD and Tytler D (1994), Dec. Atomic data for absorption lines from the ground level at wavelengths greater than 228Å. *Astronomy and Astrophysics Supplement Series* 108: 287–340.
- Viel M, Haehnelt MG and Springel V (2004), Nov. Inferring the dark matter power spectrum from the Lyman α forest in high-resolution QSO absorption spectra. *Monthly Notices of the Royal Astronomical Society* 354 (3): 684–694. doi:10.1111/j.1365-2966.2004.08224.x. astro-ph/0404600.
- Werk JK, Prochaska JX, Tumlinson J, Peebles MS, Tripp TM, Fox AJ, Lehner N, Thom C, O'Meara JM, Ford AB, Bordoloi R, Katz N, Tejos N, Oppenheimer BD, Davé R and Weinberg DH (2014), Sep. The COS-Halos Survey: Physical Conditions and Baryonic Mass in the Low-redshift Circumgalactic Medium. *The Astrophysical Journal* 792 (1), 8. doi:10.1088/0004-637X/792/1/8. 1403.0947.
- Werner N, Finoguenov A, Kaastra JS, Simionescu A, Dietrich JP, Vink J and Böhringer H (2008), May. Detection of hot gas in the filament connecting the clusters of galaxies Abell 222 and Abell 223. *Astronomy and Astrophysics* 482 (3): L29–L33. doi:10.1051/0004-6361/200809599. 0803.2525.
- Weymann R (1965), Nov. Diffusion Approximation for a Photon Gas Interacting with a Plasma via the Compton Effect. *Physics of Fluids* 8 (11): 2112–2114. doi:10.1063/1.1761165.
- White SDM and Rees MJ (1978), May. Core condensation in heavy halos: a two-stage theory for galaxy formation and clustering. *Monthly Notices of the Royal Astronomical Society* 183: 341–358. doi:10.1093/mnras/183.3.341.
- Wiersma RPC, Schaye J and Smith BD (2009), Feb. The effect of photoionization on the cooling rates of enriched, astrophysical plasmas. *Monthly Notices of the Royal Astronomical Society* 393 (1): 99–107. doi:10.1111/j.1365-2966.2008.14191.x. 0807.3748.
- Wisotzki L, Bacon R, Brinchmann J, Cantalupo S, Richter P, Schaye J, Schmidt KB, Urrutia T, Weilbacher PM, Akhlaghi M, Bouché N, Contini T, Guiderdoni B, Herenz EC, Inami H, Kerutt J, Leclercq F, Marino RA, Maseda M, Monreal-Ibero A, Nanayakkara T, Richard J, Saust R, Steinmetz M and Wendt M (2018), Oct. Nearly all the sky is covered by Lyman- α emission around high-redshift galaxies. *Nature* 562 (7726): 229–232. doi:10.1038/s41586-018-0564-6. 1810.00843.
- Wolfe AM, Gawiser E and Prochaska JX (2005), Sep. Damped Ly α Systems. *Annual Review of Astronomy and Astrophysics* 43 (1): 861–918. doi:10.1146/annurev.astro.42.053102.133950. astro-ph/0509481.

- Zaldarriaga M, Hui L and Tegmark M (2001), Aug. Constraints from the Ly α Forest Power Spectrum. *The Astrophysical Journal* 557 (2): 519–526. doi:10.1086/321652. astro-ph/0011559.
- Zhang X, Bulbul E, Malavasi N, Ghirardini V, Comparat J, Kluge M, Liu A, Merloni A, Zhang Y, Bahar YE, Artis E, Sanders JS, Garrel C, Balzer F, Brüggem M, Freyberg M, Gatuzz E, Grandis S, Krippendorf S, Nandra K, Ponti G, Ramos-Ceja M, Predehl P, Reiprich TH, Veronica A, Yeung MCH and Zelmer S (2024), Nov. The SRG/eROSITA all-sky survey: X-ray emission from the warm-hot phase gas in long cosmic filaments. *Astronomy and Astrophysics* 691, A234. doi:10.1051/0004-6361/202450933. 2406.00105.
- Zheng Z and Miralda-Escudé J (2002), Apr. Self-shielding Effects on the Column Density Distribution of Damped Ly α Systems. *The Astrophysical Journal Letters* 568 (2): L71–L74. doi:10.1086/340330. astro-ph/0201275.